Comprehensive Bulk and Single-Cell RNA Sequencing Uncovers Senescence-Associated Biomarkers in Therapeutic Mesenchymal Stem Cells

Emese Pekker[1,2*], Erda Qorri[1,3*], Márton Zs. Enyedi[4,5], Valéria Szukacsov[6], Ferhan Ayaydin[7,8], Éva Szabó-Kriston[6], Bernadett Csányi[4], Mónika Mórocz[1], Farkas Sükösd[9], Endre Kiss-Tóth[6,10,11], Lajos Haracska[1,4,6,11**]

[1]HCEMM-HUN-REN BRC Mutagenesis and Carcinogenesis Research Group, Institute of Genetics, HUN-REN Biological Research Centre, Szeged

[2]Doctoral School of Interdisciplinary Sciences, Faculty of Medicine, University of Szeged, Szeged

[3]Doctoral School of Biology, Faculty of Science and Informatics, University of Szeged, Szeged

[4]Delta Bio 2000 Ltd., Szeged

[5]Single Cell Omics Advanced Core Facility, Hungarian Centre of Excellence for Molecular Medicine, Szeged

[6]Stem CellX Therapeutics Ltd., Szeged

[7]Hungarian Centre of Excellence for Molecular Medicine (HCEMM), Functional Cell Biology and Immunology Advanced Core Facility, University of Szeged, Szeged

[8]Agribiotechnology and Precision Breeding for Food Security National Laboratory, Institute of Plant Biology, HUN-REN Biological Research Centre, Szeged

[9]Department of Pathology, Péterfy Sándor Street Hospital, Budapest

[10]Division of Clinical Medicine, School of Medicine and Population Health, University of Sheffield, Sheffield

[11] Stem CellX Ltd., Sheffield

*These authors have contributed equally to this study and share first authorship.

24   **Corresponding author. E-mail: haracska.lajos@brc.hu

25   **Abstract**

26   **Background**: Mesenchymal stem cells (MSCs) hold great promise in cell therapy, but their

27   effectiveness declines with repeated cell divisions due to senescence. Canines, sharing aging

28   characteristics with humans, serve as a valuable model to study this process in a translational

29   context.

30   **Methods**: In the present study, we performed an in-depth characterization of senescence in

31   canine MSCs using a combination of morphological, molecular, and transcriptomic analyses.

32   Early (P2) and late-passage (P6) canine MSCs were characterized using a combination of

33   senescence-associated β-galactosidase staining, cell cycle profiling, and both bulk and single-cell

34   RNA sequencing to capture global transcriptional changes.

35   **Results**: By employing a passage-based *in vitro* approach, the present study demonstrates that

36   late-passage cells (P6) compared to early-passage cells (P2) exhibit hallmark features of

37   senescence, including morphological alterations, elevated SA-β-galactosidase activity, and

38   considerable transcriptional changes. These changes were represented by significant upregulation

39   of established senescence marker genes, alongside potential novel candidates and

40   downregulation of genes associated with cell cycle progression and proliferation. Moreover,

41   single-cell RNA sequencing uncovered heterogeneous distribution of senescent subpopulations,

42   upregulation of SASP-related genes and reduced proliferation markers.

43   **Conclusions**: Our findings demonstrate that combining classical markers with bulk and single-

44   cell RNA sequencing facilitates senescent cell identification while improving quality control for

45   clinical MSC samples.

46   **Keywords**: Senescence, Mesenchymal stem cell, Animal model, Transcriptomics, Biomarkers

47   **Background**

48   Accumulating evidence suggests that mesenchymal stem cells (MSCs) present a promising

49   option for cell-based therapy. This is attributed to their multipotent differentiation potential, self-

50   renewal capability, extended *ex vivo* proliferation, paracrine potential, and immunoregulatory

51   effects[1, 2]. The characterisation of MSCs' therapeutic features has revealed significant insights

52   into their regenerative capacity, which has important implications for developing efficient

53   treatments for a wide variety of degenerative conditions[3, 4]. MSCs' distinctive characteristics

54   make them valuable tools in tissue engineering and regenerative medicine; however, the

55   beneficial functions of MSCs decline with age, a condition which may lead to organ failure and

56   age-related diseases, due to the loss of tissue homeostasis[5, 6].

57   Despite the presence of MSCs in various tissues, their abundance in the body is relatively

58   limited. Typically, cell therapy protocols require a minimum of 20–100 million MSCs per

59   treatment for autologous transplantation. Consequently, after isolation, *in vitro* expansion of

60   MSCs is required for a period ranging from four to eight weeks before transplantation[7].

61   Therefore, an adequate number of these cells can be acquired for administration only after

62   expanding them *in vitro* over several population doublings (PDs)[8, 9]. Unfortunately, the

63   proliferative capacity of MSCs decreases during culture expansion[10]. A decreasing division

64   capacity is one sign of '*in vitro* aging'. While embryonic stem cells maintain their proliferative

65   potential *in vitro*[11] and murine MSCs typically do not exhibit signs of *in vitro* senescence[12],

66   human MSCs have shown maximal population doublings of 38-40[13] *in vitro*. At a certain level

67   of PD, MSCs reach the Hayflick limit, cease to proliferate, and enter a senescent state[14].

68   Therefore, cellular senescence might affect a substantial number of cells during prolonged *in*

69   *vitro* cultivation. This process is characterized by irreversible growth arrest, which arises from a

70   variety of cellular stresses, such as telomere attrition, DNA damage, oxidative stress, and

71   activation of oncogenes[15]. Senescent cells display alterations in gene expression, including

72   increased expression of cyclin-dependent kinase inhibitors, such as p16 and p21. Senescent cells

73   also exhibit an increase in the lysosomal enzyme senescence-associated-β-galactosidase (SA-β-

74   gal) activity and reduced expression of the nuclear lamina Lamin B1 (LMNB1)[16]. Moreover,

75   senescent cells undergo significant changes in their secretome, releasing pro-inflammatory

76   factors, such as growth factors, cytokines, chemokines, and proteases, collectively known as the

77   senescence-associated secretory phenotype (SASP)[17],[18],[19]. Under normal physiological

78   conditions, SASP factors play a crucial role in tissue repair by orchestrating the recruitment of

79   immune cells and facilitating the removal of damaged tissues[20]. Nevertheless, these secreted

80   factors can induce senescence in the surrounding cells through paracrine signalling, creating an

81   inflammatory microenvironment in their vicinity[21]. MSCs are well-known to exhibit anti-

82   inflammatory properties, whereas senescent MSCs manifest evident pro-inflammatory effects

83   attributed to SASP factors[22]. SASP-related inflammation may contribute to the reduced

84   effectiveness and adverse outcomes of MSC therapies, particularly in elderly patients, driving a

85   debate over their safety and optimal application[23].

86   Cellular senescence, as an aging mechanism, is a conserved phenomenon across various

87   species[24]. Dogs represent a particularly valuable model for human aging research due to their

88   anatomical and physiological similarities to humans, as well as greater homology in DNA and

89   protein sequences compared to traditional laboratory animals like mice and rats[25]. In addition,

90   canine MSCs (cMSCs) exhibit a somewhat faster rate of PD compared to human MSCs

91   (hMSCs)[26], with a PD time of approximately two days.[27] Research in this area has gained

significant interest due to the proinflammatory role of cellular senescence in the clinical application of MSCs, as well as the potential of dogs as an ideal model for identifying novel senescence biomarkers relevant to human aging.

Efforts to characterize senescence biomarkers have identified several markers and techniques. These approaches encompass the assessment of phenotypic changes, cytogenetic techniques, and analyses of genomic and epigenomic profiles[28]. SA-β-gal activity serves as the predominant biomarker for evaluating replicative senescence under *in vitro* conditions, although it is not completely specific[29]. False positive results are caused by confluency, serum starvation, and operator bias[30]. Despite extensive efforts to characterize senescent cells, the identification of reliable and specific senescence markers remains challenging, as existing panels require further optimization to adequately capture the full complexity and heterogeneity of the senescent phenotype[31]. Cellular senescence has been previously described to occur in a tissue-specific manner, and the use of a panel of markers, rather than a single marker, has been proposed for more precise detection of senescent cells. Additionally, high-throughput sequencing methods, such as single-cell/nucleus RNA sequencing, hold great potential for uncovering heterogeneity within senescent cell populations[32].

In this study, we employed a passage-based *in vitro* approach of replicative senescence by culturing cMSCs until replicative exhaustion. With the advancement of molecular techniques, such as bulk RNA sequencing and single-cell RNA sequencing, we sought to investigate the differential gene expression profiles between late-passage cMSCs exhibiting senescent phenotype and early-passage cMSCs. The study aimed to identify potential novel biomarkers and provide a comprehensive characterisation of the heterogeneous nature of replicative senescence at the single-cell level.

Methods

MSC expansion and sample collection for the targeted assays

cMSCs were extracted from visceral adipose tissue acquired as surgical waste from healthy dogs

that received all routine vaccinations and were regularly examined by a veterinarian. The

surgical waste was provided by the veterinarian, with informed consent obtained from dog

owners, following standard ovariectomy of the clinically healthy female mixed-breed dogs.

Following the isolation of stromal vascular fraction (SVF) according to the methodology

previously described by Kriston-Pál et al.[33], the cells were grown in DMEM/F12 containing

10% foetal bovine serum (FBS) and 50 U/ml penicillin and streptomycin (all provided by

Thermo Fisher Scientific, Waltham, Massachusetts, USA). Replicative senescence was induced

in the cell culture through serial passaging, involving the progressive subculturing of cells from

passage two (P2) through passage six (P6). The cell cultures were grown up to 80% confluence

for the six consecutive passages; a medium replacement was performed every three days. Cells

were collected from each passage and subsequently stored in liquid nitrogen until processing.

Cell samples underwent assessment for mycoplasma contamination in accordance with the

procedures outlined in our prior publication[34]. Proliferating P2-derived cells and P6-derived

cells, which underwent replicative senescence, were selected for the study from a 13- month-old

donor dog. A total of 10^6 cells from both P2 and P6 were collected in triplicates for bulk RNA

sequencing from the same donor dog. Subsequently, 10^6 cells derived from P2 and P6 were

subjected to single-cell sequencing. In order to determine inter-donor consistency, another dog

isolate was also collected and subjected to single-cell sequencing utilizing the methods described

above. To evaluate the consistency and generalizability of the observed transcriptomic profiles

of early-passage cells, we also included early-passage cells from five additional dog donors.

138 These supplementary samples were used to determine whether the transcriptional signatures

139 identified in the primary isolate were representative of early-passage cells derived from other

140 individuals. Demographic information of canine isolates used in the study is presented in

141 Supplementary Table 1.

142 **Tracking morphological changes and calculating population doubling**

143 The morphological changes of the cells were monitored at each passage stage by observing the

144 cells under an EVOS FLoid microscope (Thermo Scientific), and images were captured using

145 transmitted light imaging. PD of each passage was calculated using the formula:

146 $\log_{10}(N/N_0) \times 3.33$, where N is the final cell number and N_0 is the initial number of cells plated.

147 Cumulative PD was determined by summing the PDs of each individual passage.

148 **SA-β-gal assay**

149 To evaluate senescence of MSCs, SA-β-gal staining was carried out using the SPiDER-βGal kit

150 (Dojindo), according to the manufacturer's recommendations. A total of 10^5 cells from P2 and P6

151 were cultured in triplicates in standard 6-well plates containing coverslips. To minimize the risk

152 of false-positive results caused by confluency, the cells were fixed 24 hours post-culture using

153 8% paraformaldehyde (diluted in PBS) for 10 minutes at room temperature, followed by three

154 washes with distilled water. For the detection of SA-β-gal, SPiDER-βGal stock solution was

155 diluted 2000 times in McIlvaine buffer (pH 6.0) containing 40 mM citrate-phosphate buffer, 5

156 mM potassium ferricyanide, 5 mM potassium ferrocyanide, 150 mM sodium chloride, 2 mM

157 magnesium chloride, and distilled water. The cells were incubated in the SPiDER-βGal solution

158 for 40 minutes at 37°C. Nuclei of the cells were stained with DAPI (0.1 mg/ml in PBS) after

159 washing. Coverslips were removed from the plates, drained briefly, and mounted on standard

160   microscope slides using Fluoromount-G antifade mounting medium (Southern Biotech,

161   Birmingham, USA).

162   **Confocal laser scanning microscopy**

163   Images of SPiDER-βGal- and DAPI-stained cells were acquired with a Leica Stellaris 5 (Leica

164   Microsystems CMS GmbH, Germany) confocal laser scanning microscope using 405 nm laser

165   (DAPI) and 501/525 nm laser lines of white light laser (SPiDER-βGal) with tunable emission

166   filters set to 420–487 nm and 537–614 nm, respectively. Images were taken with an HC PL APO

167   CS2 20× (N.A. 0.75) objective using the Leica Application Suite version X (LAS-X,

168   4.4.0.24861) software. Identical microscope settings were used for all intensity comparison

169   images. Average SPiDER-βGal intensities were measured using FIJI software (Image J).

170   Fluorescence intensities were measured using ROI manager, employing a macro tool to draw

171   fixed sized circles according to the code provided by Wayne Rasband on forum.image.sc

172   (https://forum.image.sc/t/changing-point-tool-to-circle-tool/26035/3, accession date:

173   24.06.2024). Two 30-pixel radius circles were drawn to measure intensities at two different

174   regions of the cytoplasm. For each measurement, a corresponding background intensity was

175   recorded outside the cell, and the actual cellular fluorescence value was normalized to this

176   background. Fluorescence intensity was quantified from exported images (ten randomly selected

177   cell images per replicate) using Fiji (ImageJ) software. Quantitative fluorescence intensity data

178   were collected from 35 cells, with measurements taken from two cytoplasmic regions per cell,

179   yielding a total of 70 measurements per replicate (Supplementary Table 2).

180   **Assessment of Replicative Potential in BrdU-labelled Cells by Immunofluorescence**

181 Actively growing MSC cells were seeded onto sterile 22 × 22 mm glass coverslips placed in 6-

182 well tissue culture plates at a density sufficient to reach approximately 60-70% confluency the

183 following day. Cells were pulse-labelled with 10 µM 5-bromo-2′-deoxyuridine (BrdU; Sigma-

184 Aldrich) for 24 h to mark actively replicating cells. After labelling, coverslips were transferred

185 (cell side up) to new 6-well plates and washed once with phosphate-buffered saline (PBS). Cells

186 were fixed in freshly prepared methanol:acetic acid (3:1, v/v) for 10 min at room temperature,

187 followed by two washes with PBS. Permeabilization was performed with PBS containing 0.5%

188 Triton X-100 (Sigma-Aldrich) for 10 min. To denature DNA and expose incorporated BrdU,

189 cells were treated with 2.5 N HCl for 1 h at room temperature. Subsequently, cells were washed

190 with 0.5 ml of 0.1 M sodium tetraborate ($Na_2B_4O_7$, Sigma-Aldrich; pH 8.5) and incubated for an

191 additional 30 min in the same buffer to neutralize residual acid. Coverslips were then washed

192 twice with PBS. Non-specific binding sites were blocked with 5% horse serum and 0.5% Triton

193 X-100 in PBS for 30 min at room temperature. Cells were incubated with mouse anti-BrdU

194 primary antibody (B44 clone; Becton Dickinson, #347580) diluted 1:300 in blocking solution

195 (100 µl per coverslip) and covered with Parafilm to prevent evaporation. The incubation was

196 carried out for 2 h at room temperature. After incubation, coverslips were washed sequentially

197 with PBS and with 1% horse serum/0.2% Tween 20 in PBS. The secondary antibody, Alexa

198 Fluor 488–conjugated goat anti-mouse IgG (Abcam, ab150113), was diluted (diluted 1:400) in

199 blocking solution and applied for 2 h at room temperature. Cells were then washed with PBS and

200 PBS containing 0.2% Tween 20. Finally, coverslips were inverted (cell side down) onto

201 microscope slides using DAPI-containing mounting medium (Fluoromount-G with DAPI;

202 Thermo Fisher Scientific, #00-4959-52). Samples were imaged using using Axioscope Z2

203 fluorescent microscope (Zeiss, Germany) with a 10x, 20x 40×objective. A minimum of 500 cells

204 from multiple microscopic fields were analysed, and the mean percentage of BrdU-positive cells

205 was plotted.

Characterisation of cell cycle stages

207 After incubation in complete growth medium, cells were trypsinized and washed with phosphate-

208 buffered saline (PBS). After washing, cells were resuspended in PBS and centrifuged at 500 rcf

209 for 10 min. After the first centrifugation step, 100% ethanol was added dropwise to the pellet,

210 which was then resuspended in PBS. After the second centrifugation step at 500 rcf for 10 min,

211 the cell pellet was resuspended in RNase solution (100 µg/ml) and PBS. Propidium iodide (1

212 mg/ml) was added to the cell suspension which was then analysed using the CytoFLEX S flow

213 cytometer (Beckman Coulter). A total of 10000 cells were gated based on forward scatter area

214 (FSC-A) versus side scatter area (SSC-A) dot plots. Singlets were identified and gated using PE

215 versus PE-A dot plots.

RNA isolation for bulk RNA sequencing and quantification

217 RNA was extracted from three parallel samples obtained from passages 2- and 6-derived cells

218 (10^6 cells each) using the RNeasy kit (Qiagen, Hilden, Germany), following the manufacturer's

219 recommendations. Quantification of extracted RNA was performed using the Qubit® 2.0

220 Fluorometer (Invitrogen, Milan, Italy) and the Qubit® RNA HS Assay Kits (Life Technologies,

221 Carlsbad, CA). Total RNA samples were quality checked with a BioAnalyzer 2100 instrument

222 using the Agilent RNA 6000 Nano Kit (Agilent Technologies USA, Cat. No. 5067-1511). The

223 RNA integrity number (RIN) values obtained were as follows: passage 2 - replicate 1: 8.60,

224 replicate 2: 9.50, replicate 3: 9.60; passage 6 - replicate 1: 8.40, replicate 2: 9.30, replicate 3:

225 8.10.

Library construction and quality control for bulk RNA sequencing

Next-generation sequencing (NGS) library preparation was carried out on 500 ng RNA for each

sample, using the NEBNext Ultra™ II Directional RNA Library Prep Kit for Illumina (NEB

#E7760) with NEBNext Poly(A) mRNA Magnetic Isolation Module (NEB #E7490).

Sequencing-ready libraries were quality control checked with a BioAnalyzer2100 instrument

using High Sensitivity DNA Chip (Agilent Technologies USA, Cat. No. 5067-4626). NGS was

carried out on the NextSeq 500 sequencing system with NextSeq 500/550 Mid Output Kit v2.5

(150 Cycles) chemistry (Illumina, Inc. USA, Cat. No. 20024904) targeting 20M reads/sample.

Bulk RNA sequencing data processing

The quality of the raw data was assessed using FastQC (v0.11.9)[35]. Adapter sequences and

low-quality reads were removed using FASTP (v0.12.4)[36]. The cleaned paired-end reads were

pseudo-aligned to the *Canis lupus familiaris* reference transcriptome (CanFam3.1 build, Ensembl

release 99) using *kallisto quant* (v0.46.1) with default parameters[37]. Quality control of the raw

data and pseudoalignment metrics can be found in the Supplementary Table 3A. The reference

transcriptome index was generated with the *kallisto index* command. Transcript abundance

estimates were summarized to gene level using the tximport package[38], filtered with the

filterByExpr function (edgeR)[39], and normalized using the trimmed mean of M-values (TMM)

method in edgeR[39]. Differential gene expression analysis was performed using limma-

voom[40], and genes with a log2 fold change (log2FC) > 1 and adjusted p-value < 0.01 were

considered significantly differentially expressed. These genes were used as input for the Gene

Ontology analysis.

247   Gene overrepresentation analysis was performed using the enrichGO function from the

248   clusterProfiler package[41]. Fold enrichment values for each GO term were calculated according

249   to the formula provided in the clusterProfiler article[41] and then ranked from highest to lowest.

250   For the KEGG enrichment analysis, the *search_kegg_organism*function was first used to retrieve

251   the KEGG abbreviation for *Canis lupus familiaris*, and the *enrichKEGG* function was then

252   utilized to identify enriched pathways in the dataset, with significant pathways determined by a

253   p-value cutoff of 0.05.

254   To assess whether the transcriptome profiles of our early-passage-derived (P2) samples are

255   similar to other early-passage cells from five different dog donors, we performed a Transcripts

256   Per Million (TPM)-based correlation analysis. The reads from passage 3-derived samples from

257   five different donors were pseudo-aligned to the reference *Canis lupus familiaris* transcriptome

258   (Ensembl release 99) using Kallisto with default settings. The resulting TPM values were then

259   compared to those from passage 2 and its technical replicates.

260   Preparation of single-cell suspensions for single-cell sequencing

261   Cryovials containing 10^6 cells were removed from liquid nitrogen storage and immediately

262   thawed in water bath at 37°C for 1 min. Subsequently, cell suspensions were transferred to 10 ml

263   of warm complete medium (DMEM/F12 containing 10% foetal bovine serum (FBS) and 50

264   U/ml penicillin and streptomycin) and centrifuged at 300 rcf for 5 min. After discarding the cell

265   supernatant, cell pellet was resuspended in 10 ml of complete medium. Following another

266   centrifugation and removal of the supernatant, 1 ml of 1x PBS + 0.04% BSA was gently added to

267   the cell pellet and resuspended. After centrifugation, a cell concentration of 700 cells/µl was

268   achieved by resuspending the pellet in 1x PBS + 0.04% BSA. Cell concentration and viability

269   were assessed following the initial and third centrifugation steps using Bürker chamber by

270   diluting the cells with trypan blue. After adjusting the cell concentration of the single-cell

271   suspension to 700 cells/µl, it was loaded into the Chromium Controller system (10x Genomics,

272   Pleasanton, CA, USA), targeting 10000 cells/sample. mRNA capture, cDNA amplification, and

273   library construction were conducted according to the manufacturer's instructions using Single

274   Cell 3′ GEM, Library & Gel Bead Kit v3.1 (10x Genomics, 1000269). The generated mRNA

275   libraries were sequenced using the Illumina NovaSeqX Plus system, targeting 20000 read pairs

276   per cell.

277   **Single-cell read mapping and quantification**

278   Raw single-cell data was processed using the Cell Ranger (v.7.2.0) software by 10x

279   Genomics[42]. Reads were aligned to the *Canis lupus familiaris* Cfam3.1 genome (updated on

280   2019-11-19), retrieved from the Ensembl database[43]. Quality metrics of this process are

281   accessible in Supplementary Table 3B. The filtered feature-barcode matrices were processed in R

282   (version 4.4.1)[44] using the Seurat package (version 4.4.0)[45]. To ensure high quality data for

283   downstream analysis, only those cells with ≥550 detected genes, ≥650 unique molecular

284   identifiers (UMIs), and less than 10% mitochondrial contamination were retained. We then

285   performed a gene-level filtering to reduce noise from lowly expressed genes. Specifically, we

286   excluded genes with zero counts, and among the remaining ones, retained only those expressed

287   in ≥10 cells for downstream analyses.

288   After filtering, data normalization was performed using the *NormalizeData* function with default

289   settings. To identify the principal components (PCs) contributing most to variance, the Seurat

290   object was scaled with the *ScaleData* function, followed by principal component analysis (PCA).

291   The data were then clustered using the *FindNeighbours* and *FindClusters* functions, and the

292   clusters were visualized using the Uniform Manifold Approximation and Projection (UMAP)

293   technique. Multiple resolutions (0.2, 0.4, 0.6, 0.8, 1.0, and 1.4) were tested to determine the

294   optimal number of subclusters, and a resolution of 0.2 was selected following a close visual

295   inspection and consideration of the study's objectives.

296   To identify genes expressed in each cluster from the P2 and P6 samples, the *FindAllMarkers*

297   function was used with thresholds of Log fold change (logFC) > 1 and adjusted p-value < 0.05

298   for marker gene selection.

299   Additionally, to ensure reproducibility and allow for cross-donor comparison of the identified

300   markers, a second single-cell RNA-sequencing run was performed on a second dog donor and

301   analysed independently, using the pipeline described above. After data quality assessment, only

302   cells with ≥650 UMIs and ≥550 detected genes were retained for further analysis

303   (Supplementary Table 4). Clustering was performed on the first ten principal components, and

304   UMAP was applied to visualize the separation of cells according to the origin of the sample.

305   Following this analysis, both runs were merged into a single Seurat object and integrated to

306   correct for technical variation using Seurat's canonical correlation analysis (CCA) framework

307   with SCTransform normalization (3000 variable features). The merged object was split by donor

308   and passage identity: P2-R1 and P6-R1 (Donor1/Run1) and P2-R2 and P6-R2 (Donor2/Run2).

309   Final integration was performed using 30 principal components, which provided optimal

310   alignment between equivalent passages, while preserving clear biological differences between

311   early and late passages. Cells were subclustered at a resolution of 0.2, and the contribution of

312   each passage to the resulting clusters was visualized using barplots. Mitochondrial transcripts

313   were excluded during the preprocessing of the second run; to ensure consistency, mitochondrial

314   genes were also excluded from the filtered object of the first run prior to integration.

Analysis of publicly available datasets

To investigate the expression patterns of the identified senescence markers across different organisms, the datasets from Casella et al. (2019)[46] (GEO ID: GSE130727) and Wang et al. (2022)[47] (GEO ID: GSE179880) from human and mice samples, respectively, were analysed. The analysis was carried out as previously described in the section "Bulk RNA-sequencing data analysis", with significance thresholds set according to the criteria reported in the respective publications.

An additional single-cell RNA-sequencing dataset from Fard et al.[48] (2023: GEO accession GSE200157) was included in the analysis. From the available samples, only the T0 and T2 time points were retrieved and compared. Droplets were initially filtered using DropletUtils[49] and quality control was performed as previously described applying the following thresholds: UMIs $\geq$ 600, features $\geq$ 500 and $\leq$ 6000, and mitochondrial content < 20%. The filtered data were normalized using SCTransform and integrated with Harmony[50] based on 30 principal components. The expression levels of the selected markers were subsequently examined using dot plots.

Statistical Analyses and Software

The differences in β-gal activity between P2 and P6 were assessed using the Wilcoxon Rank Sum test. Prior to analysis, data distribution was visually inspected and formally tested for normality using the Shapiro-Wilk test. As the data do not follow a normal distribution, Wilcoxon Rank Sum test was selected. All statistical analyses including the Spearman rank correlation analysis of the TPM expression profiles were performed in R (version 4.4.1). Additionally, visualizations, including PCA, donut charts, and volcano plots were generated using the

337   ggplot2[51] and EnhancedVolcano packages[52]. Heatmaps were generated using the pheatmap

338   package unless otherwise specified. Workflows and figure panels were assembled using

339   BioRender.

340   For the BrdU experiments, statistical differences between P2 and P6 were evaluated using an

341   unpaired t-test. Prior to analysis, data normality was assessed using the Shapiro–Wilk test, which

342   confirmed that the samples did not significantly deviate from a normal distribution. Therefore, an

343   unpaired t-test was applied to determine differences between the samples. The mean values

344   obtained from microscopic field counts were plotted with standard deviations.

Cell cycle analysis

346   To determine the cell cycle stage of the cells in both samples, the *CellCycleScoring* function

347   from Seurat was utilized[45]. The function calculates enrichment scores for the S and G2M

348   phases, assigning each cell to one of three phases: G2M, S, or G1. Cells with negative scores for

349   both the G2M and S phases are classified as G1 cells[53]. The list of human cell cycle marker

350   genes compiled by Tirosh, I. et al. was retrieved from Seurat[54]. For *Canis lupus familiaris*, the

351   cell cycle gene list was generated through ortholog searches using the guidelines provided in the

352   tutorial https://github.com/hbc/tinyatlas. Based on the cell cycle classification, the percentage of

353   cells in each phase (G1, S, and G2M) was calculated.

Co-occurrence analysis

355   To identify novel senescence-related markers, we devised a co-occurrence approach based on the

356   hypothesis that a cell must express key senescence markers (cited in over 20 scientific

357   publications on cellular senescence) such as CCND1, IGFBP2, CDKN1A, TGFB2, along with at

358   least one of the top ten genes upregulated in P6 (CDKN2A, IGFBP7, CRYAB, ITGA2, PTN,

359   NDUFA4L2, COL11A1) identified through the *FindAllMarkers* function. After identifying these

360   cells, we calculated the percentage of senescent cells within each subcluster.

361

362   **Results**

363   **cMSCs undergoing replicative senescence display altered cell morphology and increased β-**

364   **galactosidase activity.**

365   Proliferating MSCs from P2 were cultured until P6, where they reached replicative exhaustion,

366   leading to cellular senescence. P2 cells exhibited a population doubling level (PDL) of 2.7 over a

367   7-day culture period, whereas P6 cells showed a PDL of 0.75 over a 14-day culture period

368   (Supplementary Figure 1), reaching a cumulative PDL of 8.67. Proliferating cells derived from

369   P2 and P6-derived cells undergoing replicative exhaustion were selected for the present study.

370   We observed that late-passage cells derived from P6 exhibited enlarged and flattened

371   morphology, characteristic of senescent cells, in contrast to the P2-derived proliferating cells

372   (Supplementary Figure 2). Cellular senescence was confirmed by investigating the senescent

373   phenotype of the P6-derived cells; P2 and P6 cells were treated with Spider β-Gal. In P6-derived

374   cells, an increase in fluorescence signal was observed, indicating replicative senescence.

375   Representative images can be seen in Figure 1A. A significantly increased β-galactosidase

376   activity was observed in P6 cells compared to P2 cells, increasing from 6.8 in P2 to 40.3 in P6

377   (Figure 1B).

378

379
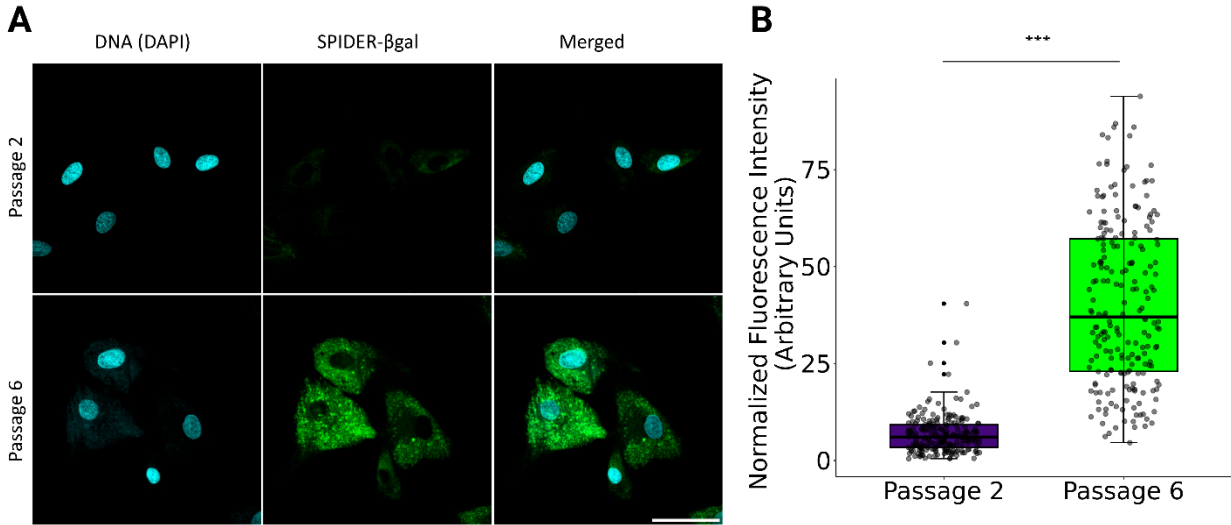
Figure 1 SA-β-gal assay. A. Representative images of SA-β-gal staining assay. Scale bar is 50

μm **B.** Quantitative fluorescence intensity data were obtained from 35 cells, measuring two

cytoplasmic regions per cell, resulting in a total of 70 measurements per replicate. For each

measurement, background fluorescence outside the cell was recorded and used for normalization.

The boxplot whiskers extend from the third and first quartiles to the largest and smallest values,

respectively, within 1.5 x the interquartile range (IQR), where IQR represents the range between

the first and third quartiles.

The observed difference in fluorescence intensity was considered statistically significant, with a

p-value <2.2e-16.

To further validate these observations, we next assessed proliferative capacity using the BrdU

incorporation assay. Analyses were performed at passages 2 and 6, once cultures reached 50–

60% confluence to ensure comparable growth conditions. Consistent with the β-galactosidase

results, BrdU incorporation revealed a pronounced reduction in proliferation with increasing

passage number: 82% of P2 cells incorporated BrdU, compared to only 25% of P6 cells (Figures

2A and 2B).

395   2A-B). This sharp decline in DNA synthesis activity confirms that late-passage MSCs undergo

396   significant proliferative arrest, which might be in line with the onset of replicative senescence.
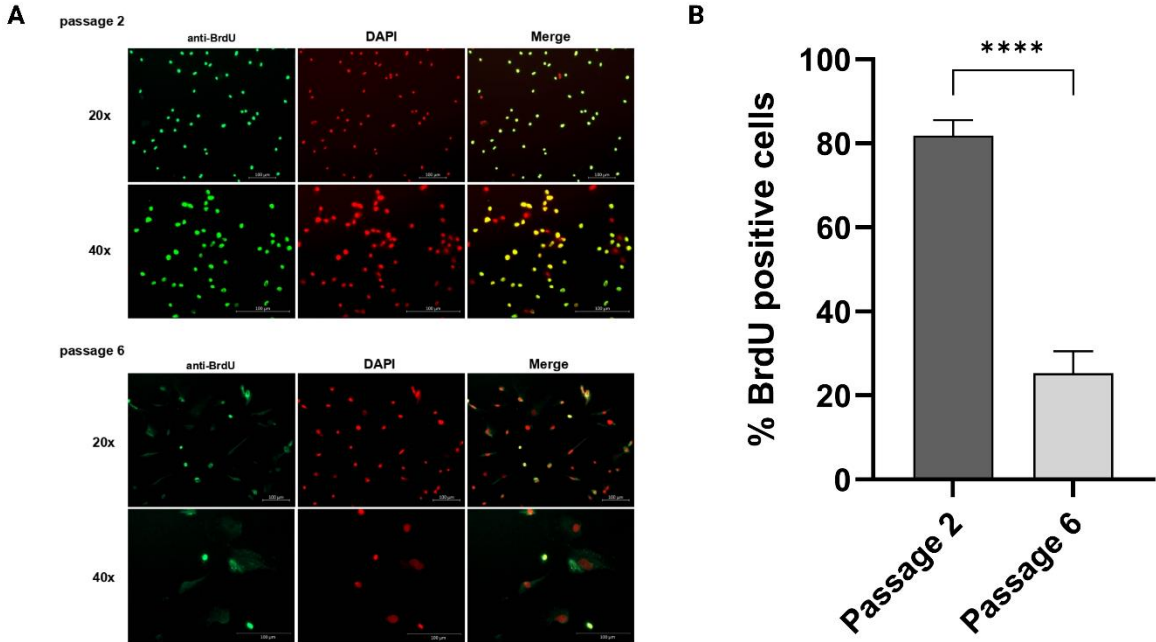
398   **Figure 2 Reduced proliferative activity in late-passage cells, determined by BrdU**

399   **incorporation**. **A.** Representative immunofluorescence images of cells at passage 2 (top) and

400   passage 6 (bottom) stained with anti-BrdU antibody (green) and DAPI (red) to visualize the

401   nuclei. Merged images show BrdU-positive nuclei in yellow. Images were acquired at 20× and

402   40× magnifications. Scale bars: 100 μm. **B.** Quantification of BrdU-positive cells expressed as a

403   percentage. Data represents the mean ± standard deviation from microscopically counted fields.;

404   ****$p < 0.0001$.

405   **Comprehensive profiling of differentially expressed genes (DEGs), associated processes,**

406   **and pathways in MSC senescence**

407   To evaluate replicative senescence-mediated gene expression changes in MSCs, we initially

408   carried out bulk RNA sequencing. MSCs were harvested across six consecutive cell passages,

19

409   with cells from passages P2 and P6 chosen for detailed analysis. Bulk RNA sequencing was

410   performed on P2- and P6-derived cells in triplicates, following RNA extraction and library

411   preparation, using the Illumina NextSeq 500 platform. The sequencing data were subsequently

412   subjected to comprehensive bioinformatic analysis (Figure 3A). The gene expression profiles of

413   MSCs derived from P6 were compared to those of P2-derived cells using three independent

414   experimental replicates. Principal Component Analysis (PCA) revealed a clear separation

415   between the early- and late-passage samples (Supplementary Figures 3A and 3B). A total of

416   1091 genes were identified as DEGs, including 533 upregulated genes (Supplementary Table 5)

417   and 558 downregulated genes (Supplementary Table 6 and Figure 3B).

418   Among the upregulated DEGs, the most prominent were NEFH, VCAM1, LHX1, MECOM,

419   ADGRB1, CPA4, TIE1, HOXA13, C1QL1, ANKRD1, and NKX2-5, along with two

420   unannotated transcripts (ENSCAFG00000044398 and ENSCAFG00000031632). Among these,

421   the NEFH (neurofilament heavy chain) gene exhibited the highest logFC, with a value of 7.12.

422   CCND1 (Cyclin D1), CDKN1A (Cyclin Dependent Kinase Inhibitor 1A), and CDKN2A (Cyclin

423   Dependent Kinase Inhibitor 2A) also showed significant upregulation in P6, reflecting cell cycle

424   arrest. In contrast, BNC1 (Basonuclin Zinc Finger Protein 1) exhibited the most pronounced

425   decrease in expression levels (logFC = -7), along with GAS7, SELENOP, LSP1, PREX1,

426   ABCC9, COL24A1, WT1, COL4A5, CD36, FBN2, THSD4, CPXM1, PDGFD, and PAX8,

427   indicating diminished metabolic and extracellular matrix activity, consistent with loss of

428   proliferative capacity. The top differentially expressed genes based on log2FC values are

429   illustrated in Figure 3B, with downregulated DEGs shown on the left and upregulated DEGs on

430   the right.

431   To determine the similarity between the transcriptome profiles of our early-passage-derived (P2)

432   samples and early-passage cells from five different dog donors, we conducted a correlation

433   analysis based on TPM values. Spearman rank correlation revealed that the P2 samples show

434   strong correlations ($\geq$0.96) with P3 samples from five different dog donors (Supplementary

435   Figure 4), suggesting that the transcriptome profiles of early-passage cells are highly similar to

436   those of passage 3-derived cells. Overall, these results indicate that the transcriptomic profile of

437   our early-passage-derived (P2) samples is comparable to early-passage cells from other dog

438   donors, supporting their reliability and consistency for further analysis.

439   To assess the functional significance of the DEGs, we performed GO and KEGG enrichment

440   analyses separately for up- and downregulated genes. Downregulated genes showed significant

441   enrichment in 142 GO terms (Supplementary Table 7), primarily related to cell cycle regulation

442   and DNA replication, consistent with reduced proliferative capacity (Figure 3C). In contrast, the

443   178 enriched GO terms for upregulated genes (Supplementary Table 8) were linked to ERK

444   signalling, hypoxia response, cell differentiation, and neurogenesis, reflecting response to

445   replicative stress of these cells (Figure 3D).
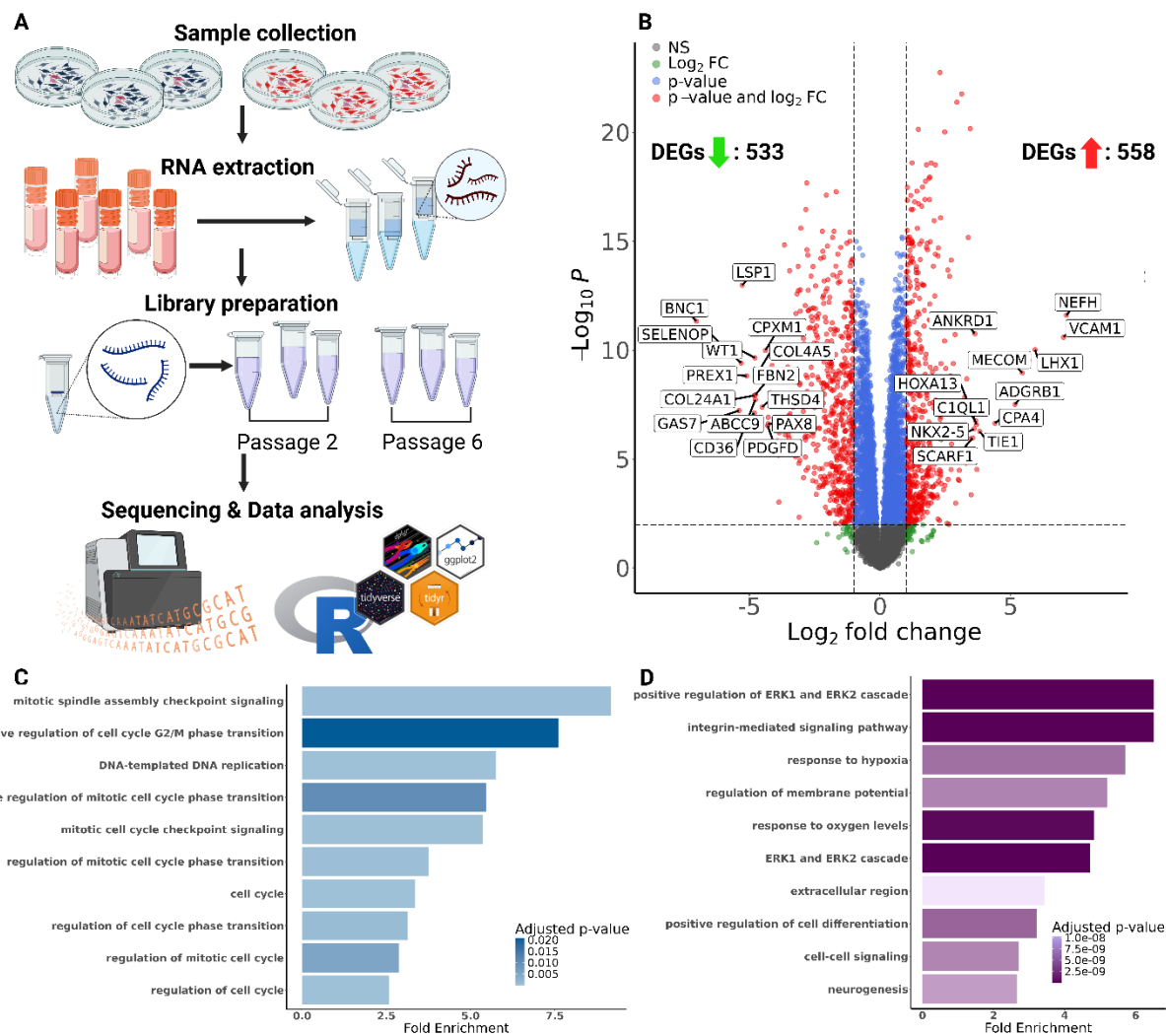
Figure 3 Bulk RNA sequencing-based transcriptomic analysis. A. Schematic representation

of the workflow for bulk RNA seq-based assay**.** MSCs were collected from six consecutive cell

passages. P2- and P6-derived cells were selected for the study. Bulk RNA sequencing of P2- and

P6-derived cells was carried out in triplicates, following RNA extraction and library preparation

using Illumina NextSeq 500, and the results were analysed bioinformatically. Created in

BioRender. Kiss, E. (2025) https://BioRender.com/2i3n4gv. **B.** Volcano plot highlighting the top

identified DEGs in P6-derived samples, compared to P2 samples. Red data points indicate those

genes that were significantly upregulated (right) or downregulated (left). X-axis=Log_2FC,

455 horizontal dashed line indicates cutoff for P-value<0.01, while the vertical dashed lines indicate

456 the cutoff for fold change of 2. **C.** Results of GO enrichment analysis for the downregulated

457 differentially expressed genes. X-axis = Fold enrichment values. Y-axis=relevant enriched GO

458 terms for different biological processes; colour intensity of bars based on p-value. **D.** Results of

459 GO analysis for the upregulated DEGs. X-axis = Fold enrichment values. Y-axis=relevant

460 enriched GO terms for different biological processes; colour intensity of bars based on p-value.

461 To further examine the functions of the identified differentially expressed genes within specific

462 pathways, we conducted KEGG pathway analysis. A total of 23 pathways exhibited significant

463 enrichment, among which 15 were linked to the upregulated DEGs (Supplementary Table 9).

464 Notably, the most significantly enriched pathways included hypertrophic cardiomyopathy, dilated

465 cardiomyopathy, and hematopoietic cell lineage. Additionally, the HIF-1 signalling pathway, the

466 PI3K-Akt signalling pathway, and pathways related to cancer also demonstrated significant

467 enrichment. The downregulated DEGs were assigned to eight pathways (Supplementary Table

468 10); among them, DNA replication, cell cycle and progesterone-mediated oocyte maturation

469 showed the highest representation.

470 **UMAP analysis reveals distinct clustering of early and late passage cMSCs**

471 To investigate the molecular mechanisms underlying the heterogeneity in MSC senescence, we

472 performed a comprehensive single-cell transcriptomic analysis on cMSCs subjected to

473 replicative senescence. To characterize the differences between senescent cells from P6 and

474 actively dividing cells from P2, as well as the heterogeneity within the senescent cell population,

475 we conducted single-cell gene expression profiling using the specific 10x Single Cell 3′ GEM

476 pipeline, and subsequently caried out sequencing using the Illumina NovaSeqX Plus system

477 (Figure 4A).

23

478 UMAP analysis of the dataset comprising cells derived from P2 and P6 unveiled the presence of

479 eight distinct clusters (see Figure 4B) organized in two major cell populations. Subsequent

480 plotting of cells according to the origin of the sample demonstrated that the two major cell

481 populations are represented by a distinct separation between early-passage cells and late-passage

482 senescent cells (Figure 4C). The early-passage cell population (P2) predominantly comprised

483 clusters 0, 3, 4, and 7, while the late-passage cell population (P6) was dominated by clusters 1, 2,

484 5, and 6. Cells in clusters 0, 3, 4, and 7 constituted 99.7%, 77.5%, 99.2%, and 100%,

485 respectively, of the P2-derived cell population. Cells in clusters 1, 2, 5, and 6 comprised 99.3%,

486 99.6%, 99.3%, and 99.6%, respectively, of the cells derived from P6, suggesting considerable

487 differences in the transcriptional profile of early- and late-passage cell populations. Details are

488 shown in Supplementary Figure 5.

489 The housekeeping genes Actin Beta (ACTB), Beta-2-Microglobulin (B2M), Glyceraldehyde-3-

490 Phosphate Dehydrogenase (GAPDH), and Phosphoglycerate Kinase 1 (PGK1) were analysed

491 across the clusters, and all were found to be expressed throughout (Supplementary Figure 6). The

492 number of cells expressing the abovementioned genes per cluster can be found in Supplementary

493 Table 11. Expression of established MSC markers – CD44, THY1 (CD90), FN1, ALCAM,

494 ITGB1 (CD29), and ENG (CD105) – was detected across the clusters, supporting the origin and

495 identity of the analysed MSC cell populations (Supplementary Figure 7).

496

24

497
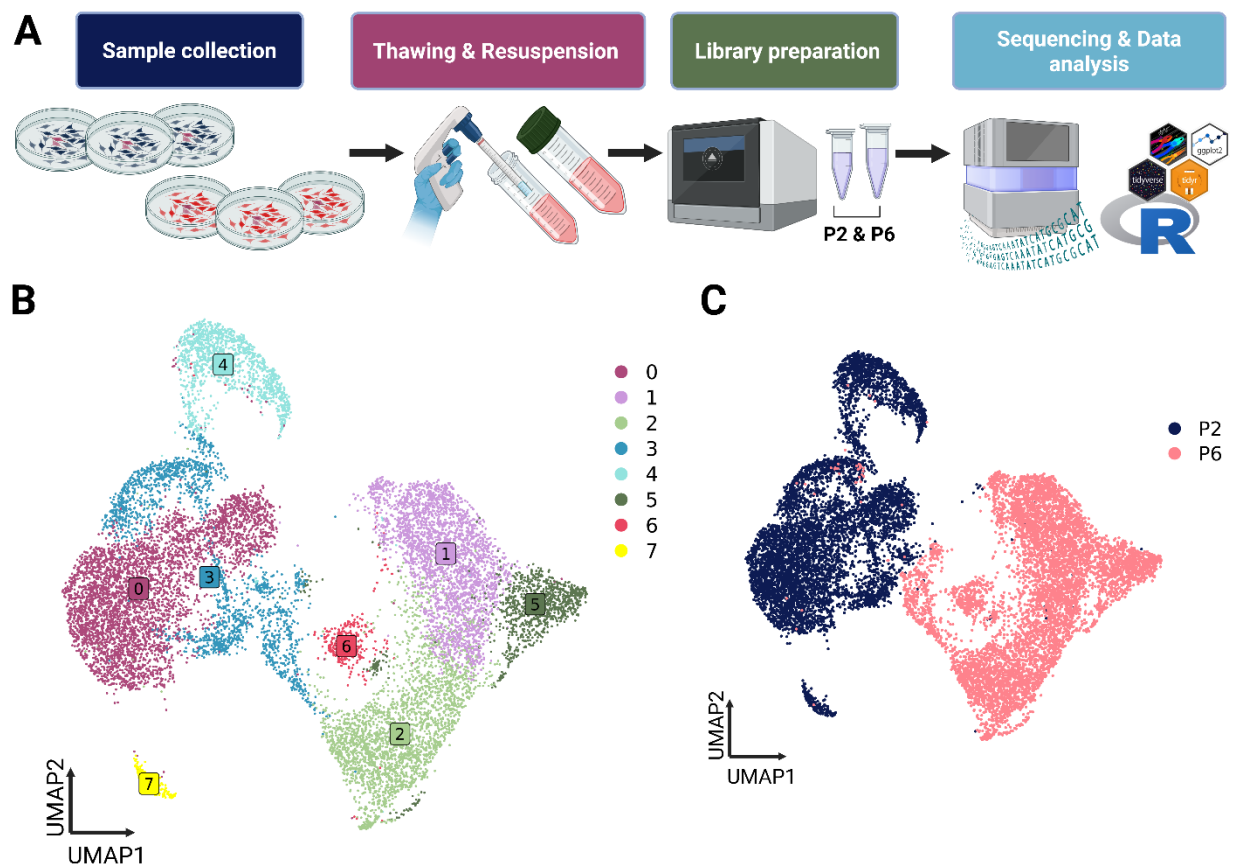
**Figure 4 Single-cell RNA sequencing workflow and UMAP clustering analysis of cells derived from P2 and P6. A.** MSCs were collected from six consecutive cell passages, and P2- and P6-derived cells were selected. Single-cell RNA sequencing was carried out using Single Cell 3′ GEM, Library & Gel Bead Kit v3.1 and sequenced using the Illumina NovaSeqX Plus system, and the results analysed bioinformatically. Created in BioRender. Kiss, E. (2025) https://BioRender.com/lncnz90. **B.** Distribution of the identified clusters. **C.** Distribution of the clusters based on the origin of the sample (P2= Passage 2, P6= Passage 6).

Cell cycle stages and proliferative properties of actively dividing and senescent cMSCs at the single-cell level

25

507   One of the main senescence-associated features includes cell cycle arrest of cells in the G1

508   phase. To evaluate cell cycle arrest during the emergence of replicative senescence, flow

509   cytometry was performed. P2- and P6-derived cells were collected and stained with propidium

510   iodide. The cells were subsequently analysed using flow cytometry. As shown in Figure 5A, P6

511   cells exhibited a marked increase in G1 phase accumulation (83.2%) compared to P2 cells

512   (71.5%).

513   We further employed the *CellCycleScoring* function in the Seurat package to conduct cell cycle

514   analysis and identify the distribution of G1-arrested senescent cells across clusters (Figure 5B),

515   using transcriptomic signatures specific to distinct cell cycle phases. In line with flow cytometry

516   results, cell scoring estimated that 67.31% of cells derived from P6 were in the G1 phase

517   compared to 55.2% of cells from P2 (Figure 5C). Consistent with this, the specific late-passage

518   clusters (clusters 1, 2, 5, and 6) demonstrated diminished expression of transcripts for cell

519   proliferation markers and division regulators, including PLK1 (Figure 5D), MKI67, and MCM3,

520   and displayed decreased expression for MCM6, further supporting that subsets within these cell

521   populations were likely not undergoing active division. Notably, PLK1, MKI67, and MCM3

522   were expressed exclusively in cluster 3 from the early-passage cell population, while MCM6

523   exhibited elevated expression relative to clusters 0, 4, and 7 within the early-passage cells,

524   further underscoring that cluster 3 is characterized by a high proportion of proliferating cells

525   (Figure 5E). These results strongly indicate that P6-derived cells are predominantly G1-arrested,

526   whereas early-passage P2 cells exhibit elevated expression of the proliferation marker MCM6.

527   Additionally, early-passage P2 cells include a specific cluster with pronounced expression of cell

528   proliferation markers and division regulators, supporting the active proliferative status of these

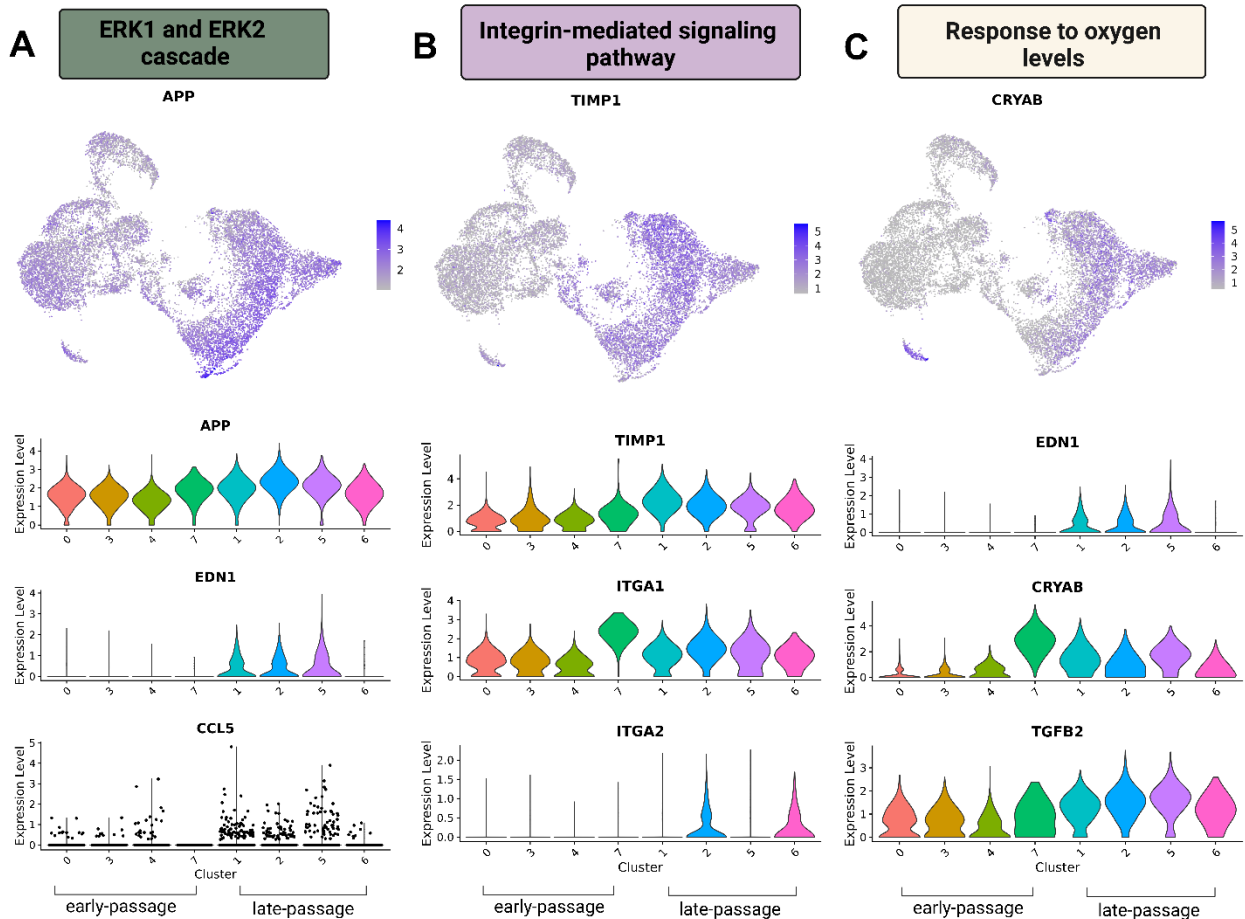529   cells from cluster 3.

530

531
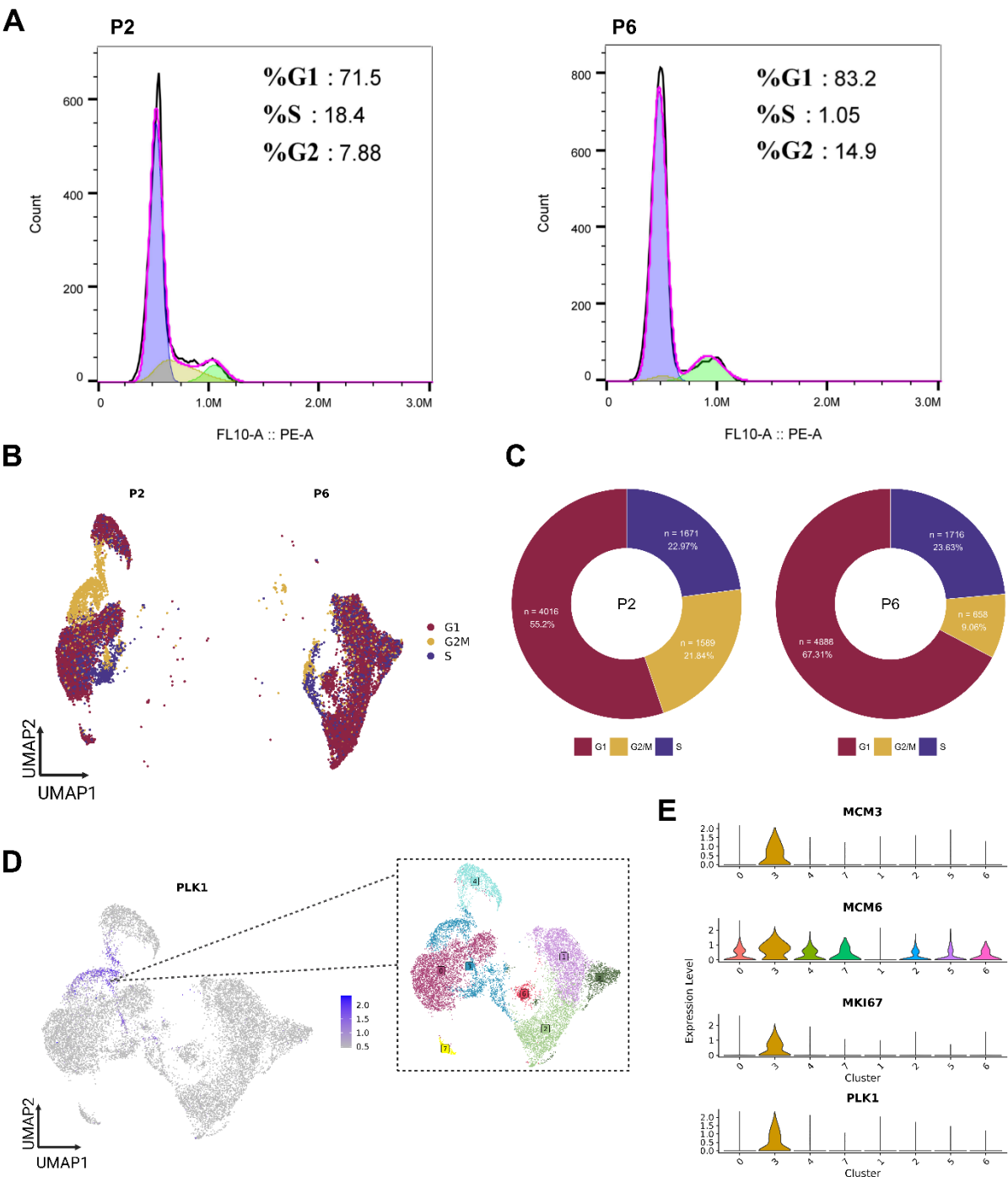
Figure 5 Cell cycle stages and proliferation dynamics within the clusters. A. The cell cycle of

the sorted cells was assessed by flow cytometry using propidium iodide staining. Representative

27

534   images of P2 (left) and P6 (right) cells are shown, highlighting that P6 cells are represented by a

535   considerably higher proportion of cells in the G1 phase. **B-C**. Cell cycle stages of the cell

536   population and percentages are displayed separately for P2 (left) and P6 (right), as determined by

537   Cell Scoring analysis using the Seurat package. **D**. Feature plot representing the expression of

538   proliferation marker PLK1 among the clusters. Inset on the right highlights cluster distribution **E.**

539   Expression of transcripts for cell proliferation markers and division regulators PLK1, MKI67,

540   MCM3, and MCM6. The clusters are arranged based on the origin of the sample (P2 followed by

541   P6).

542   **Evaluation of senescence-related pathways in cMSCs**

543   We evaluated the expression of genes associated with the enriched GO terms identified through

544   bulk RNA sequencing, focusing on three key pathways highly relevant to cellular senescence: the

545   ERK1 and ERK2 cascade, the integrin-mediated signalling pathway, and response to oxygen

546   levels. Consistent with the observations from bulk RNA sequencing, the late-passage cell

547   populations represented by clusters 1, 2, 5, and 6 showed elevated expression of the ERK1 and

548   ERK2 cascade-related genes APP, EDN1, and CCL5. Notably, cluster 6 showed reduced

549   expression of EDN1 and CCL5 compared to other late-passage clusters (Figure 6A). Another

550   important significantly enriched GO term in P6 samples was the integrin-mediated signalling

551   pathway. Single-cell analysis revealed elevated expression of the pathway-associated genes

552   TIMP1, ITGA1, and ITGA2 in specific late-passage clusters. Interestingly, ITGA1 exhibited

553   higher expression in cluster 7, while ITGA2 was more prominently expressed in clusters 2 and 6

554   (Figure 6B). Elevated oxygen concentrations frequently trigger the onset of senescence,

555   underscoring the significance of oxygen level responses in cellular senescence[55]. The

556   expression profiles of genes associated with the oxygen-response pathway demonstrated elevated

557　levels in clusters derived from P6, notably including TGFB2. However, EDN1 exhibited

558　downregulation in cluster 6. Additionally, CRYAB was most highly expressed in cluster 7

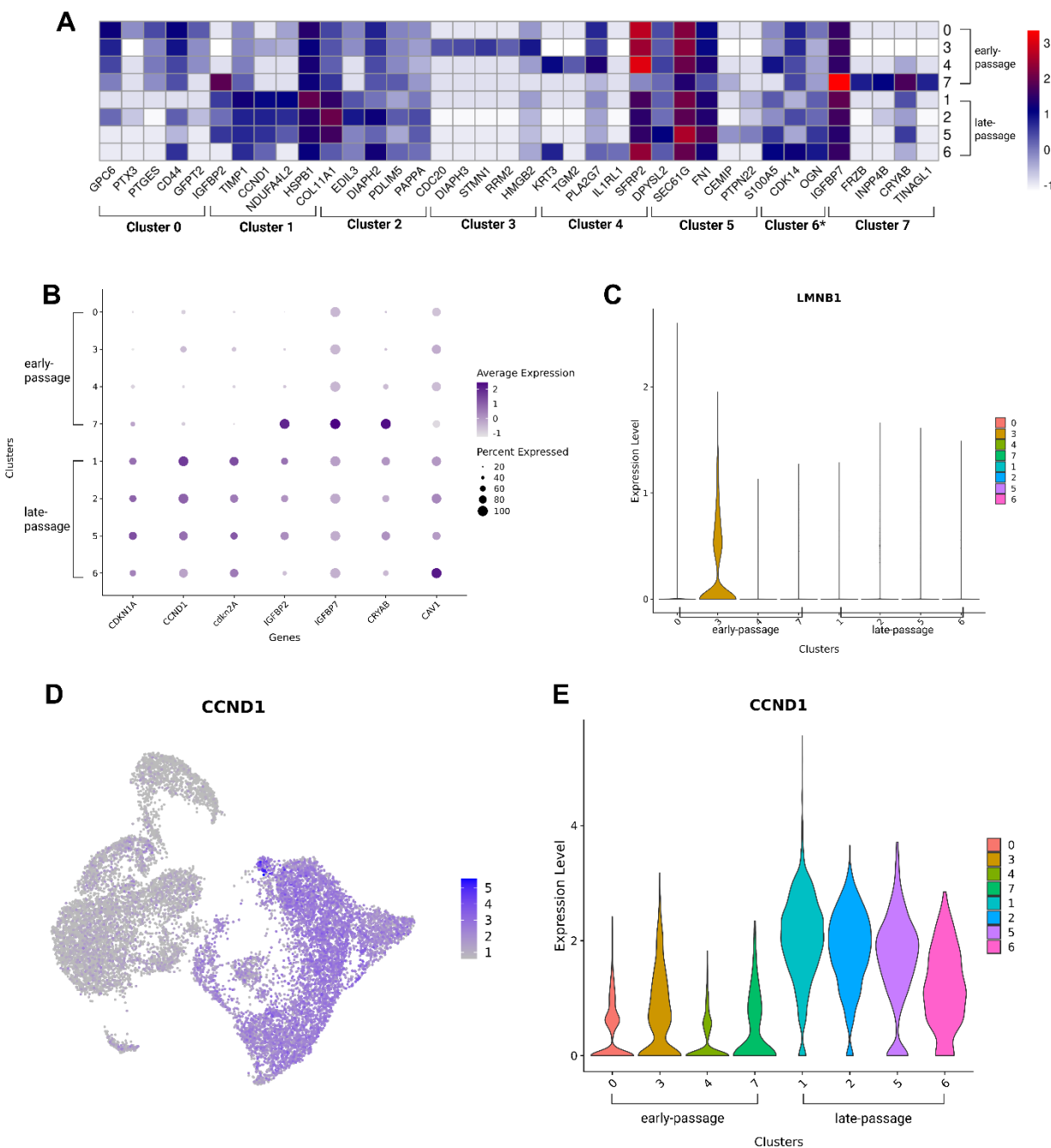559　(Figure 6C).

560

561

562　**Figure 6 Evaluation of the significantly enriched GO terms, emphasizing three critical**

563　**pathways associated with cellular senescence at the single-cell level**. **A.** the ERK1 and ERK2

564　cascade: feature plot illustrating the expression of the APP gene (top), violin plots showing the

565　expression levels of the ERK1 and ERK2 cascade-related genes APP, EDN1, and CCL5 among

566　the clusters (bottom). **B**. Integrin-mediated signalling pathway: feature plot illustrating the

567   expression of the TIMP1 gene (top), violin plots showing the expression levels of the integrin-

568   mediated signalling pathway-related genes TIMP1, ITGA1, and ITGA2 (bottom). **C.** Response

569   to oxygen levels: feature plot illustrating the expression of the CRYAB gene (top), violin plots

570   showing the expression levels of response to oxygen levels GO term-related genes EDN1,

571   CRYAB and TGFB2 (bottom). The clusters are arranged based on the origin of the sample (P2

572   followed by P6).

573   **Characterisation of the unique transcriptional profiles of clusters and identification of**

574   **shared senescence-associated and SASP-related signatures**

575   To characterize the transcriptional profiles of the clusters, we employed the *'FindAllMarkers'*

576   function to identify genes with the highest representation uniquely associated with each cluster

577   (details are shown in Supplementary Table 12). Remarkably, cluster 3 exhibited a distinct

578   transcriptional signature, characterized by the top five highly expressed genes that showed

579   diminished expression in the other clusters. These included CDC20, a key regulator of the

580   metaphase-to-anaphase transition during cell division, DIAPH3, which influences cell motility

581   and adhesion, STMN1, which modulates signals of the cellular environment, and RRM2 and

582   HMGB2, involved in cell proliferation, demonstrating that cells from cluster 3 are engaged in

583   active cell division and proliferation. Late-passage cell clusters 1, 2, 5, and 6 exhibited

584   transcriptomes associated with cellular senescence. These clusters demonstrated elevated

585   expression of several components of SASP, including IGFBP2, IGFBP7, and PAPPA, as well as

586   the senescence-related genes CCND1 and CRYAB. However, the expression of IGFBP2 was

587   reduced in cells from cluster 6, whereas IGFBP7 displayed prominent expression in cluster 1

588   derived from P6, with notably high levels of these SASP factors also detected in cluster 7.

589   CCND1 exhibited strong expression in P6 clusters 1, 2, 5, and 6, while CRYAB showed

590   prominent expression in clusters 1 and 5, with particularly high levels observed in cluster 7.

591   Interestingly, OGN (Osteoglycin), described as a negative regulator of cellular senescence[56],

592   exhibited elevated expression across all late-passage clusters (1, 2, 5, and 6). The top five

593   identified marker genes are represented in Figure 7A.

594

595   **Figure 7 Characterization of cluster-specific markers and assessment of transcriptional**

596   **patterns of genes associated with cellular senescence. A.** Heatmap showing the top five highly

597   expressed marker RNAs in each cluster (based on LogFC). Cluster6*: Genes KRT3 and IL1RL1

598   appear in the top five marker list for both cluster 4 and cluster 6. To avoid redundancy and

599   potential confusion, the expression values of these genes were visualized under cluster 4 and

600   were excluded from the visualization for cluster 6. Median expression levels were plotted for

601   cells in each cluster. Colour represents expression intensity (based on LogFC value). The clusters

602   are arranged based on the origin of the sample (P2 followed by P6), whereas the genes are

603   arranged based on cluster order from cluster 0 to 7. **B.** Dotplot depicting markers commonly

604   associated with cellular senescence, with dot colour representing the average RNA expression

605   levels scaled across all clusters. The size of each dot indicates the percentage of cells expressing

606   a specific RNA within each cluster. The clusters are arranged based on the origin of the sample

607   (P2 followed by P6). **C.** Violin plot depicting the expression of LMNB1. **D.** Feature plot

608   depicting the expression of CCND1. **E.** Violin plot showing the expression level of CCND1 for

609   each cluster. The clusters are arranged based on the origin of the sample (P2 followed by P6).

610

611   We further evaluated the expression of several genes commonly associated with the hallmarks of

612   cellular senescence. Notably, senescence-associated genes encoding the proteins p21

613   (CDKN1A), p16 (CDKN2A), and cyclin D1 (CCND1) were overexpressed in the late-passage

614   cell clusters. The SASP factors IGFBP2 and IGFBP7 displayed increased expression in cluster 7;

615   however, IGFBP2 was downregulated in the other P2-derived clusters, while IGFBP7

616   demonstrated consistent expression across all remaining clusters. Additionally, the newly

617   identified robust senescence marker CRYAB was also significantly overexpressed in cluster 7.

618   Furthermore, CAV1, a gene known to play a critical role in cellular senescence, exhibited marked

619   upregulation in cells from cluster 6 (Figure 7B). Loss of LMNB1 was proposed to be associated

620   with cellular senescence[57, 58], and, in line with this, our study revealed a pronounced

621   downregulation of LMNB1 expression in late-passage cell clusters; interestingly, with a similar

622   reduction in early-passage-derived clusters 0, 4, and 7. However, as shown in Figure 7C,

623   LMNB1 expression remained consistently high in cluster 3, a population of actively proliferating

624   cells. Among these identified genes, CCND1 was one of the core genes exhibiting elevated

625   expression levels in all late-passage clusters compared to early-passage clusters (Figures 7D and

626   E).

627   **Inter-cluster comparison reveals distinct gene expression profiles of late-passage cMSCs**

628   To gain deeper insight into the transcriptomic profiles of late-passage-derived senescent cells and

629   their distribution, we conducted an inter-cluster comparison between early-passage and late-

630   passage cell clusters. Specifically, transcriptional profiles of early-passage clusters (0, 3, 4, 7)

631   were compared to those of late-passage clusters (1, 2, 5, 6) to identify differential gene

632   expression patterns associated with cellular senescence. This approach allowed us to explore the

633   distinct transcriptional signatures potentially contributing to the onset and progression of

634   senescence, providing a clearer understanding of the molecular shifts that occur during cellular

635   aging at the single-cell level. The comparison yielded a total of 3,319 differentially expressed

636   genes; among these, the ten genes exhibiting the highest expression levels (as determined by

637   logFC values), along with the ten most significantly downregulated genes (Supplementary Table

638   13), are presented in Figure 8A. Commonly recognized markers of cellular senescence including

639   CCND1, IGFBP2, CDKN1A, CDKN2A, and TIMP1 were considerably overexpressed in the

640   late-passage clusters. Moreover, CRYAB, an important senescence-related gene and novel

33

641   senolytic target[59, 60], also showed elevated expression in the late-passage clusters.

642   Interestingly, CRYAB, along with IGFBP2, presented considerable enrichment in cluster 7,

643   suggesting that the early-passage-derived cells constituting this cluster may also be in a

644   senescent state.

645   We also evaluated the expression levels of the genes most significantly downregulated in P6,

646   identified by their lowest logFC values, and from the top five marker genes of cluster 3, four

647   were among them: CDC20, DIAPH3, STMN1, and RRM2, indicating that cluster 3 also plays an

648   important role in driving the differences between early and late-passage cell populations. Several

649   key genes involved in fundamental cellular processes were also downregulated in the late-

650   passage clusters. These include FBLN1, which promotes osteogenesis[61]; MYBL2, a critical

651   regulator of cell cycle progression; RACGAP1, a gene that regulates cytokinesis, cell growth,

652   and differentiation; TK1, essential for DNA replication; the transcription factor ZNF608; and

653   HPCAL1, which has been shown to promote glioblastoma cell proliferation[62] (Figure 8A). We

654   further investigated the expression profiles of the novel senolytic target, CRYAB and its

655   interacting partners across the cell clusters. As previously highlighted, CRYAB exhibited marked

656   overexpression in the late-passage clusters, but with cluster 7 showing the most pronounced

657   upregulation. Additionally, CRYAB's interacting partners APP and HSPB1 were also

658   overexpressed in late-passage clusters relative to early-passage ones. Notably, APP demonstrated

659   elevated expression in cluster 2, while HSPB1 showed substantial overexpression in cluster 1.

660   Interestingly, HSPB2 expression was upregulated in cluster 7, further supporting the senescence-

661   associated phenotype observed in this cluster (Figure 8B).

662

Figure 8 Analysis of top marker genes in late-passage cell populations and characterisation of CRYAB-interacting partners. A. Heatmap showing the expression of the top ten marker

665 genes in late-passage cell populations. Each line represents a single cell, the colour indicates the

666 expression level (pink – downregulated, yellow – overexpressed). The clusters are arranged

667 based on the origin of the sample (P2 followed by P6). **B.** Ridge plot of CRYAB expression and

668 its interacting partners APP, HSPB1, and HSPB2. **C.** Bar graph displaying the percentage of

669 putative senescent cells across clusters, based on gene co-occurrence analysis. The analysis

670 includes both established senescence markers and newly identified genes that may serve as

671 potential novel markers of cellular senescence. The clusters are arranged based on the origin of

672 the sample (P2 followed by P6).

673 Building on these results, we aimed to assess our approach by quantifying the proportion of

674 candidate senescent cells within each cluster. Therefore, a gene co-occurrence analysis was

675 performed under the hypothesis that a cell must express core senescence markers – specifically

676 CCND1, IGFBP2, CDKN1A, and TGFB2 – alongside at least one of the top ten genes

677 (CDKN2A, IGFBP7, CRYAB, ITGA2, PTN, NDUFA4L2, COL11A1) upregulated in P6 as

678 identified through inter-cluster comparison of early- and late-passage cell clusters. The gene co-

679 occurrence analysis revealed a pronounced increase in the proportion of putative senescent cells

680 within late-passage clusters compared to early-passage ones (Figure 8C). Specifically, clusters 0,

681 3, 4, and 7 in early-passage cells contained 2.4%, 8.7%, 3.6%, and 17% senescent cells,

682 respectively. In contrast, the late-passage clusters 1, 2, 5, and 6 showed markedly higher

683 proportions of these cells, with 48.4%, 52.6%, 60.8%, and 25.5%, respectively (Supplementary

684 Table 14).

685 **Comparative analysis of senescent and actively dividing subpopulations reveals distinct**

686 **proliferative and secretory signatures**

687 To further examine the heterogeneity among senescent subpopulations, we focused on clusters 3

688 and 7, which differ in both cellular composition and senescence-associated gene expression.

689 Cluster 3 contains a mixture of early- and late-passage cells, whereas cluster 7 is composed

690 primarily of early-passage cells that nevertheless display pronounced SASP activity and

691 senescence signatures. To elucidate the molecular distinctions between these cell groups and

692 their relationship to senescence progression, we performed an inter-cluster comparison. This

693 analysis revealed that cluster 3 exhibits strong expression of proliferation-associated genes (e.g.,

694 MYBL2, RRM2, HMGB2, CDC20, STMN1), consistent with an actively dividing population. In

695 contrast, cluster 7 showed marked upregulation of CRYAB, IGFBP7, FRZB, DCN, and SASP-

696 and extracellular matrix-related genes, along with decreased expression of proliferative markers,

697 features characteristic of a senescent, secretory phenotype (Supplementary Figure 8).

698 Furthermore, to gain a deeper understanding of the mixed composition of cluster 3, which

699 contained both early- and late-passage cells, we conducted a subclustering analysis. UMAP

700 visualization revealed that cluster 3 could be further subdivided based on passage number and

701 the expression of proliferation-related genes. Cells from passage 2 and passage 6 formed largely

702 distinct subgroups with minimal overlap, indicating that passage number is a major contributor to

703 the heterogeneity observed within cluster 3 (Supplementary Figure 9A-D). Within these

704 subclusters, the differential expression of proliferation-associated genes PLK1, MKI67, and

705 MCM3 was evident. Certain subpopulations exhibited high expression of these markers, whereas

706 others showed lower expression levels, suggesting reduced proliferative activity. This refined

707 subclustering thus underscores the intrinsic heterogeneity within cluster 3 (Supplementary

708 Figures 9A-E).

709

Evaluation of inter-donor and inter-species consistency of the senescence-related

characteristics and identified potential marker genes

To further assess inter-donor consistency and characterize cellular phenotypes, we conducted additional analyses on a second canine isolate, including morphological examination, BrdU incorporation to evaluate proliferative capacity, and single-cell RNA sequencing combined with cell cycle analysis. Similarly to the primary samples, this isolate exhibited a marked decline in proliferation, decreasing from 84% at passage 2 to 56% at passage 6 (Supplementary Figures 10A and 10B), accompanied by an enlarged, flattened morphology characteristic of senescent cells (Supplementary Figure 11). Overall, both isolates demonstrated a pronounced reduction in replicative potential by passage 6, reflecting consistent senescence-associated phenotypes across donors.

The transcriptomic profile was further examined using single-cell sequencing. UMAP clustering revealed ten distinct cellular clusters (Supplementary Figure 12A). When coloured by sample origin (Supplementary Figure 12B), cells from passage 2 and passage 6 showed partial separation, indicating some transcriptional divergence between passages, though mixed clusters were also observed, suggesting overlap in cell states. Cell cycle phase analysis was also conducted and further demonstrated differences in the distribution of cells across G1, S, and G2/M phases between the two passages, with a pronounced enrichment of passage 6 cells in the G1 phase (76.38%) compared to passage 2 cells (43.50%) (Supplementary Figures 12 C and D). To minimize technical variation between samples, the cells from both single-cell RNA sequencing datasets were integrated for downstream analysis. Following integration, the UMAP visualization (Supplementary Figure 13A) revealed that cells from passage 2 and passage 6 each formed distinct and well-defined clusters, with cells from the two sequencing runs of the same

733 passage grouping together. This indicates strong consistency between replicates. A limited

734 overlap was observed between passages, which originated from the second canine isolate.

735 Clustering analysis (Supplementary Figure 13B) identified nine major cell populations, and the

736 distribution of cells across clusters (Supplementary Figure 13C) confirmed this observation,

737 highlighting transcriptomic differences between passages while showing reproducibility across

738 sequencing runs and between different donors. Next, the marker genes identified in the present

739 study were evaluated in the integrated dataset. As illustrated, the expression patterns of the

740 downregulated genes (Supplementary Figure 13D) CDC20, FBLN1, MYBL2, DIAPH3,

741 STMN1, RRM2, RACGAP1, TK1, ZNF608, and HPCAL1 and upregulated genes

742 (Supplementary Figure 13E) CCND1, IGFBP2, CDKN1A, TGFB2, CDKN2A, IGFBP7,

743 CRYAB, ITGA2, PTN, NDUFA4L2, COL11A1, and TIMP1 were consistent with those observed

744 in the first single-cell sequencing run. Specifically, the downregulated genes showed diminished

745 levels, while the upregulated genes showed elevated expression levels in the cell populations.

746 These consistent expression trends across independent sequencing runs and independent canine

747 isolates further support the inter-donor reproducibility and robustness of the findings.

748 To evaluate interspecies consistency of the identified candidate markers, we performed a

749 literature search to determine publicly available datasets suitable for comparison. We specifically

750 sought studies aligning with our experimental context of replicative senescence. Accordingly,

751 publicly available mouse and human replicative exhaustion datasets were analysed to assess the

752 expression patterns of the proposed marker genes. Differential gene expression analysis of the

753 mouse dataset, comparing late-passage (P7) to early-passage (P1) cells, demonstrated that

754 CCND1, IGFBP2, CDKN1A, CDKN2A, IGFBP7, PTN, NDUFA4L2, and TIMP1 were

755 significantly upregulated in P7 cells, consistent with the described senescence-associated

756   transcriptional profile. In contrast, ITGA2 showed downregulation, while TGFB2 and CRYAB

757   were not detected among the differentially expressed genes. Examination of the downregulated

758   markers revealed that CDC20, MYBL2, DIAPH3, STMN1, RRM2, RACGAP1, and TK1 were

759   also significantly reduced in expression, whereas FBLN1, ZNF608, and HPCAL1 did not show

760   significant differential expression between passages (Supplementary Table 15).

761   Furthermore, differential gene expression analysis of the human dataset, comparing proliferative

762   cells to cells undergoing replicative senescence, revealed that CCND1, TGFB2, IGFBP7, and

763   ITGA2 were upregulated, whereas PTN, NDUFA4L2, and COL11A1 were downregulated.

764   Among the proposed downregulated markers, FBLN1, MYBL2, STMN1, RRM2, and TK1 also

765   showed decreased expression, while HPCAL1 was the only gene displaying increased expression

766   in senescent cells (Supplementary Table 16).

767   Comparative analysis across these species revealed a total of nine genes that were significantly

768   differentially expressed in dog, human, and mouse datasets. Among these, six genes displayed

769   consistent expression patterns (either upregulated or downregulated) across all three species,

770   indicating strong interspecies conservation of senescence-associated transcriptional responses.

771   Additionally, nine genes were shared between the dog and mouse datasets, suggesting a high

772   degree of overlap in their senescence-related gene expression profiles. Detailed gene lists and

773   overlap are provided in Supplementary Figure 14.

774   In addition, single-cell RNA sequencing data from a recent study by Taherian Fard et al.

775   (2024)[48] investigating human MSC replicative senescence were analysed independently. We

776   selected all replicates corresponding to two time points: T0 (day 23) representing proliferative

777   cells and T2 (day 63) representing cells undergoing replicative senescence. This comparison

778   identified 16 genes exhibiting expression patterns consistent with our dataset, with CCND1,

779 CDKN1A, CDKN2A, CRYAB, ITGA2, NDUFA4L2, COL11A1, and TIMP1 showing

780 upregulation (Supplementary Figure 15A), while CDC20, FBLN1, MYBL2, DIAPH3, STMN1,

781 RRM2, RACGAP1, and TK1 were markedly downregulated in T2 samples (Supplementary

782 Figure 15B).

783 **Discussion**

784 In the rapidly advancing field of cell therapy, MSCs have captured considerable interest due to

785 their unique biological properties, stemness, and immunomodulatory abilities[63, 64].

786 Nevertheless, their efficacy can diminish due to replicative senescence. While a variety of

787 biomarkers and techniques have been explored to identify and characterize senescent MSCs, the

788 lack of a universally accepted, specific marker complicates reliable detection and

789 characterisation of these cells. Our study contributes to solving this issue by providing a detailed

790 analysis of the transcriptional changes associated with replicative senescence of MSCs in dog, a

791 model organism known for its key physiological similarities to humans and recognized as a

792 valuable platform for aging research[25]˙[65–67].

793 cMSCs exhibit both conserved and species-specific characteristics of senescence, reflected by

794 fundamental differences in telomere biology and cellular stress responses. In humans, replicative

795 senescence is characterized by enlarged, flattened cell morphology, strong SA-β-gal

796 accumulation, and upregulation of p16 and p21, accompanied by a broad transcriptional shift

797 toward a SASP-related phenotype[28]. On the other hand, murine MSCs may exhibit similar

798 morphological and β-gal changes but progress more slowly toward senescence, largely due to

799 their long telomeres and sustained telomerase activity[68]. Moreover, Fehrer et al. (2006)

800 observed that murine MSCs lack the classical indicators of *in vitro* senescence, showing no

801　growth arrest or SA-β-gal activity, although cells with abnormal morphology emerge at higher

802　passages[12]. However, studies have shown that the transcript for p16, encoded by the CDKN2A

803　gene, exhibits a similar age-associated increase in expression in humans and rodents[69], [70].

804　cMSCs exhibit classical features of senescence similar to human MSCs, including altered

805　morphology, reduced proliferation, and increased β-galactosidase activity[71] and also tend to

806　enter senescence more rapidly[72]. However, studies examining gene expression changes during

807　cMSC senescence remain limited. Therefore, cMSCs closely reflect human senescence and

808　support longitudinal studies in a large-animal system, positioning the dog as a highly relevant

809　model for investigating MSC senescence. In this study, we employed a passage-based *in vitro*

810　approach of replicative senescence by culturing cMSCs until they reached replicative exhaustion.

811　To this end, we compared early passage P2 and late passage P6 cells exhibiting markedly distinct

812　proliferative capacities, as clearly reflected by their respective PDLs.

813　Replicative senescence in cMSCs was first indicated by distinct morphological alterations, with

814　late-passage P6 cells exhibiting the characteristic enlarged and flattened morphology, elevated

815　SA-β-gal activity, and significantly reduced BrdU incorporation, confirming the senescent

816　phenotype, consistent with previously reported senescent phenotypes[73, 74]. Employing bulk

817　RNA sequencing to assess gene expression changes associated with replicative senescence, we

818　identified a set of significantly upregulated and downregulated genes in P6 cells compared to

819　early-passage P2 cells. Among the significantly upregulated genes, we detected well-established

820　senescence markers, including CCND1, CDKN1A, and CDKN2A. Moreover, we identified

821　genes with the highest levels of overexpression in P6 MSCs, some of which correspond to

822　known senescence-associated signatures, while others point to potentially novel associations. For

823　instance, VCAM1, which was previously described as being overexpressed in senescent

824   endothelial cells[75, 76], was significantly upregulated in our study. Among other notable genes,

825   ANKRD1 has been reported as aging-related[77] and senescence marker gene[78], while

826   MECOM has been associated with pathways relevant to senescence, cell cycle, and p53

827   signalling, as highlighted by a former study by KEGG analysis[79]. Moreover, it is important to

828   highlight that other genes such as NKX2-5, LHX1, ADGRB1, and CPA4 displayed significant

829   upregulation but lack prior associations with cellular senescence. Additionally, TIE1, shown to

830   exhibit age-independent upregulation in vascular contexts[80], and HOXA13, described as a key

831   participant in Erk1/2 activation[81, 82], may offer unique insights into cellular aging

832   mechanisms, while NEFH, a biomarker of neuronal differentiation[83], which demonstrated the

833   highest overexpression, and C1QL1, a senescence-associated gene with potential roles in

834   neuronal differentiation[84, 85], suggest potential new directions for exploration.

835   Furthermore, numerous genes linked to cell proliferation and cell cycle regulation appear

836   markedly downregulated in senescent P6 cells compared to early-passage P2 cells. Among the

837   most significantly downregulated were BNC1, a transcription factor predominantly expressed in

838   proliferative keratinocytes and germ cells[86]; SELENOP, which plays a role in Wnt pathway

839   activation and cellular proliferation[87]; LSP1, involved in the negative regulation of

840   proliferation[88]; and PREX1, which supports homeostatic proliferation[89]. Several other genes

841   including critical regulators of cell proliferation and cell cycle progression were also observed to

842   be downregulated in the senescent P6 samples, namely, TOP2A, MYBL2, MKI67, DPT, WT1,

843   and PIMREG[90–95].

844   Another defining feature of senescent cells is stable cell cycle arrest, characterized by the loss of

845   proliferative capacity. The downregulation of these genes potentially facilitates the advancement

846   of cellular senescence. The loss of LMNB1, a critical constituent of the nuclear lamina, has been

847   shown to represent another important characteristic and marker of senescent cells[16]. Consistent

848   with this, our results showed a clear and significant downregulation of this gene in the senescent

849   P6 samples.

850   Moreover, GO and KEGG enrichment analyses provided deeper insight into the biological

851   relevance of the identified DEGs in the context of senescence. Downregulated genes were

852   primarily associated with cell division and cell cycle-related processes – such as mitotic spindle

853   assembly checkpoint signalling, G2/M phase transition, and DNA replication – highlighting a

854   functional shift away from proliferation. Additional GO terms, such as regulation of the mitotic

855   cell cycle, mitotic checkpoint signalling, and cell cycle regulation, further emphasize this pattern.

856   These findings are consistent with prior research demonstrating that senescent cells commonly

857   undergo stable cell cycle arrest and reduced proliferative activity[96–98]. This evidence further

858   supports the hypothesis that late-passage P6 samples are not actively dividing and are likely in a

859   state of cell cycle arrest.

860   The analysis also highlighted significantly enriched GO terms for the upregulated DEGs

861   corresponding to biological processes closely related to and previously associated with aging and

862   cellular senescence, such as the ERK1 and ERK2 cascade[99], the integrin-mediated signalling

863   pathway[100], and response to hypoxia[101]. Moreover, the KEGG pathway analysis identified

864   key pathways that are actively studied in the context of cellular senescence, such as the HIF-1

865   signalling pathway, which is essential for response to hypoxia[102], and the PI3K-Akt signalling

866   pathway[103]. These pathways are well-established in the literature as key players in cellular

867   aging and senescence, often contributing to both cell survival and the pro-inflammatory features

868   of senescence. These findings suggest that senescence is not merely a state of arrest, but an

869   actively regulated process with significant implications for tissue homeostasis and aging.

44

870   However, during replicative senescence, cells with critically shortened telomeres trigger a DNA

871   damage response resulting in cell cycle arrest[104]. The cyclin-dependent kinase inhibitors p21

872   and p16 play crucial roles in this process by orchestrating proliferative arrest. These proteins

873   have been widely recognized as hallmark markers of senescent cells[105]. In our study, flow

874   cytometry using propidium iodide labelling, followed by single-cell analysis with

875   CellCycleScoring, revealed a pronounced accumulation of P6 cells in the G1 phase. This

876   approach provided a more sensitive and precise identification of cell cycle phases, utilizing gene

877   expression markers of proliferation. Furthermore, the expressions of the proliferation- and cell

878   division-specific markers MCM3, MCM6, MKI67, and PLK1 were assessed for the clusters. All

879   these markers were found to be downregulated in the P6 clusters. Interestingly, among P2

880   clusters, only cluster 3 showed marked expression of MCM3, MKI67, and PLK1, further

881   supporting that P6-derived cells are no longer capable of sustained division, while early-passage

882   cells, such as those in cluster 3, remain proliferatively active.

883   The development of single-cell sequencing technologies enabled us to uncover that the gene

884   expression changes identified in our study demonstrate considerable heterogeneity at the level of

885   individual cells. Therefore, the expressions of genes associated with important identified GO

886   terms – representing pathways involved in senescence, including the ERK1/ERK2 signalling

887   cascade, the integrin-mediated signalling pathway, and the cellular response to oxygen levels –

888   were also evaluated at the single-cell level. In accordance with bulk RNA sequencing results,

889   late-passage cell populations from clusters 1, 2, 5, and 6 expressed elevated levels of APP,

890   EDN1, and CCL5. However, cluster 6 demonstrated reduced expression of EDN1 and CCL5

891   compared to the other P6-derived clusters, suggesting potential differences in the activation of

892   the ERK1/ERK2 pathway within specific subpopulations. The integrin-mediated signalling

893 pathway, another significantly enriched GO term in P6 cells, showed upregulation of key genes,

894 including TIMP1, ITGA1, and ITGA2, across late-passage clusters. Interestingly, ITGA1 was

895 more highly expressed in cluster 7, while ITGA2 was prominently expressed in clusters 2 and 6.

896 Furthermore, genes involved in the cellular response to oxygen levels, a critical factor in

897 senescence induction[106], were generally upregulated in P6-derived clusters. However,

898 similarly to the pattern observed in the ERK1/ERK2 pathway, EDN1 – also included in the

899 oxygen levels GO term – was downregulated in cluster 6.

900 Kawamura et al. recently reported upregulation of TGFB2 in old MSCs compared to younger

901 MSCs[107]. Similarly, our study identified a marked upregulation of TGFB2 across all clusters

902 derived from late-passage MSCs, further supporting these observations. Furthermore, Caveolin 1

903 (CAV1), a key regulator of cellular senescence[108], which has also been shown to be

904 upregulated in response to oxidative stress[60], exhibited significant upregulation in cluster 6.

905 CRYAB also exhibited elevated expression in all P6 clusters compared to P2; intriguingly, it also

906 showed particularly high expression in cluster 7 of the P2 population. This finding further

907 supports the involvement of oxygen-related stress in senescence, as CRYAB is known to be

908 upregulated in response to oxidative stress conditions[109]. Collectively, these findings

909 underscore the complexity and heterogeneity of cellular senescence, highlighting the distinct

910 activation of senescence-related pathways across different late-passage cell populations.

911 UMAP analysis of the dataset from P2- and P6-derived cells revealed eight transcriptionally

912 distinct clusters. Visualization by cell origin demonstrated near-complete segregation between P2

913 and P6 populations; however, cluster 3 stands out as less well-defined, consisting predominantly

914 of P2-derived cells but also including a notable subset from P6, suggesting partial overlap in

915 gene expression profiles. Differences in transcriptional profiles were also observed among the

46

916   identified clusters. To characterize the clusters based on their expression profiles, we employed

917   the 'FindAllMarkers' function to identify genes that were most prominently expressed in each

918   cluster. This approach revealed considerable variation in the transcriptional patterns across the

919   clusters, offering important insights into their unique gene expression signatures. Notably, cluster

920   3 exhibited a distinct transcriptional profile, characterized by the expression of genes that play

921   crucial roles in cellular processes, including those involved in cell division and proliferation.

922   This suggests that cluster 3 comprises primarily actively dividing cells, while also containing a

923   subset of active cells from P6, further highlighting its role as a proliferative population. In

924   contrast, clusters associated with late-passage P6 cells exhibited a high representation of key

925   senescence and SASP-related genes, including TIMP1, CRYAB, CCND1, IGFBP2, IGFBP7, and

926   PAPPA. Interestingly, cluster 7, derived from P2 cells, displayed the most pronounced expression

927   of IGFBP7 and CRYAB.

928   The induction of cell cycle arrest and the onset of senescence were corroborated by evaluating

929   the expression of the cyclin-dependent kinase inhibitors p21 (CDKN1A) and p16 (CDKN2A),

930   which play critical roles in regulating proliferative arrest at the single-cell level. CCND1 is well

931   known to promote progression through the G1/S checkpoint, and its overexpression can

932   stimulate cell cycle progression or bypass arrest[110]. However, in certain contexts, CCND1

933   overexpression can paradoxically induce cell cycle arrest or senescence-like phenotypes.

934   Sustained CCND1 accumulation may result in aberrant CDK activity, activate checkpoint

935   pathways such as the p21 signalling cascade, or disrupt regulatory feedback, ultimately

936   reinforcing growth arrest rather than promoting proliferation[111]. Additionally, acute

937   overexpression of cyclin D1 (CCND1) has been demonstrated to drive cell cycle arrest in the G1

938   phase[112]. However, previous studies showed downregulation of CCND1 in senescent human

939 MSCs[113] and that its expression can counteract senescence, whereas loss of CCND1

940 accelerates senescence in certain cancer cell models[114]. This apparent discrepancy may reflect

941 context- or tissue-dependent regulation, which may account for the observed upregulation of

942 CCND1 in senescent cMSCs, despite their persistent G1 arrest.

943 Our results showed a considerable overexpression of the CDKN1A and CDKN2A genes across

944 all P6-derived clusters, as compared to P2 cell clusters. Surprisingly, SASP factors, such as

945 IGFBP2, IGFBP7, and CRYAB, which were described as an oxidative stress-related genes[109]

946 and potential senolytic target[59], exhibited substantial overexpression specifically in cluster 7.

947 The presence of these markers in a cluster originating from early-passage cells suggests that a

948 subset of P2 cells may already be undergoing stress responses or entering a pre-senescent state.

949 This observation points to a potential heterogeneity in senescence susceptibility within cluster 7,

950 originating from early-passage populations. Interestingly, we observed elevated OGN expression

951 across all late-passage cMSC clusters, despite previous reports of OGN downregulation in

952 senescent human MSCs[115] and its link to reduced osteogenic capacity in aged MSCs[116].

953 This upregulation may reflect a compensatory mechanism in cMSCs to preserve osteogenic

954 potential during senescence, also highlighting possible species- or context-dependent differences

955 in OGN regulation. Additionally, previous studies have described that the loss of LMNB1, a key

956 component of the nuclear lamina, is a prominent marker of senescent cells[16]. In line with our

957 bulk RNA sequencing results, P6 samples exhibited a clear downregulation of LMNB1.

958 Interestingly, within the P2 cell populations, only cluster 3 displayed marked expression of

959 LMNB1, a finding that further supports the proliferatively active status of the cells in this cluster.

960 Interestingly, while LMNB1 expression was downregulated across P6-derived cells, as expected

961 due to its known downregulation during senescence, its lack of pronounced expression in cluster

962 7 compared to cluster 3 further suggests that cluster 7 may be diverging from the proliferative

963 state and adopting a distinct phenotype. This intermediate or transitional state between

964 proliferation and senescence is particularly intriguing and may have significant implications for

965 understanding the onset of cellular senescence.

966 In late-passage cells, inter-cluster comparison revealed upregulation of established senescence

967 markers (CCND1, CDKN1A, CDKN2A) alongside genes previously linked to senescence

968 (IGFBP2, TGFB2, IGFBP7, ITGA2, PTN, COL11A1, TIMP1, CRYAB), while NDUFA4L2

969 appeared as a potentially novel association. Among the downregulated genes, FBLN1, DIAPH3,

970 and ZNF608 represent previously unreported candidates that may have unexplored roles in the

971 process of cellular senescence. We also showed that CRYAB's interacting partners were

972 upregulated in P6 clusters, except for HSPB2, which exhibited particularly notable

973 overexpression in cluster 7, providing additional evidence that cluster 7 might also present a

974 senescence-related phenotype. Comparative analysis of senescent and proliferative

975 subpopulations revealed distinct transcriptional patterns underlying their divergent phenotypes.

976 Cluster 3, composed of both early- and late-passage cells, showed strong expression of

977 proliferation-associated genes (e.g., MYBL2, RRM2, HMGB2, CDC20, STMN1), indicating

978 that a subset of late-passage cells also retained proliferative activity. Moreover, subclustering of

979 cluster 3 revealed that passage number was a key driver of intracluster heterogeneity, with

980 distinct subgroups emerging based on differential expression of proliferative markers. In

981 contrast, cluster 7 was characterized by marked upregulation of CRYAB, IGFBP7, and other

982 SASP- and ECM-related genes, reflecting a senescent, secretory phenotype. Notably, the

983 presence of senescence-associated markers in early-passage cluster 7 suggests that pre-senescent

984 features can emerge prior to replicative exhaustion, highlighting the intrinsic heterogeneity and

985 gradual onset of senescence within MSC populations.

986 To evaluate the reproducibility and biological relevance of these findings, we performed cross-

987 species comparisons using publicly available human and murine MSC senescence datasets. This

988 analysis revealed strong conservation of transcriptional trends across independent canine isolates

989 and consistency among species, confirming the robustness of the proposed marker panel. Gene

990 co-occurrence analysis further demonstrated a substantially higher proportion of senescent cells

991 in late-passage clusters, validating the transcriptional indicators identified.

992 Beyond providing a molecular map of MSC senescence, our findings have important

993 translational implications. The identified gene panel could guide the development of platforms

994 for monitoring MSC quality in therapeutic manufacturing. In particular, these markers could be

995 integrated into prospective quality control assays to detect early transcriptional indicators of

996 senescence before the functional decline occurs. However, translating transcriptomic signatures

997 into practical diagnostic assays will require further validation. Overall, this study provides a

998 comprehensive characterization of replicative senescence in cMSCs, revealing distinct molecular

999 states that capture the transition from proliferation to senescence. By defining both conserved

1000 and novel markers and proposing their combined use as a panel of up- and downregulated genes

1001 for MSC manufacturing and quality control, our findings bridge the gap between mechanistic

1002 discovery and clinical translation, offering a foundation for improved standardization and

1003 efficacy in MSC-based therapies.

1004 **List of abbreviations**

1005 DNA: Deoxyribonucleic acid

1006   RNA: Ribonucleic acid

1007   S phase: Synthesis phase

1008   MSC: Mesenchymal Stem Cell

1009   cMSC: Canine mesenchymal stem cell

1010   hMSC: Human Mesenchymal Stem Cell

1011   P2: Passage 2

1012   P6: Passage 6

1013   SA-β-galactosidase: Senescence-associated-β-galactosidase

1014   PD: Population doubling

1015   SASP: Senescence-associated secretory phenotype

1016   IQR: Interquartile range

1017   PCA: Principal Component Analysis

1018   DEG: Differentially expressed gene

1019   NGS: Next-generation sequencing

1020   TPM: Transcripts Per Million

1021   UMAP: Uniform Manifold Approximation and Projection

1022   **Supplementary information**

1023   All data generated or analysed during this study are included in this published article and its

1024   supplementary information files: Supplementary information and Supplementary Data.

Declarations

Ethics Approval and Consent to Participate

The owner of the dogs who participated in this study provided written informed consent.

Consent for publication

Not applicable.

Availability of data and materials

The RNA-sequencing and single-cell RNA sequencing data generated in this study have been deposited in the NCBI Sequence Read Archive (SRA) under the BioProject accession numbers PRJNA1235683 and PRJNA1235986, respectively. The data for the second single-cell RNA sequencing run are available from the following link: https://doi.org/10.5281/zenodo.17346986.

The code utilized to analyse the data and to generate the figures presented in this study are available in the GitHub repository based on the following link: GitHub - erdaqorri/Mesenchymal-Stem-Cell-CLF

Competing interests

All authors declare no financial or non-financial competing interests.

Declaration of generative AI and AI-assisted technologies in the writing process

1050 During the preparation of this work the author(s) used ChatGPT-4o in order to enhance the

1051 language quality of the manuscript. After using this tool, the author(s) reviewed and edited the

1052 content as needed and take(s) full responsibility for the content of the publication.

Authors' contributions

1054 EP contributed to the conceptualization, methodology, investigation, formal analysis, and writing

1055 – original draft manuscript, visualization. EQ contributed to methodology, bioinformatical

1056 analysis, visualization, formal analysis, and writing – original draft manuscript. MZE contributed

1057 to methodology, writing, and editing. VS contributed to methodology, writing, and editing. FA

1058 contributed to methodology, writing, and editing, ÉSK contributed to methodology. CB

1059 contributed to methodology and formal analysis. MM contributed to methodology and formal

1060 analysis. FS contributed to formal analysis and resources. EKT contributed to conceptualization,

1061 methodology, and formal analysis. LH contributed to conceptualization, formal analysis, project

1062 administration, resources, and funding acquisition. All authors read and approved the final

1063 manuscript.

Acknowledgements

1069

1070   **References**

1071

1072   1. El Omar R, Beroud J, Stoltz J-F, Menu P, Velot E, Decot V. Umbilical Cord Mesenchymal Stem Cells: The
1073   New Gold Standard for Mesenchymal Stem Cell-Based Therapies? Tissue Eng Part B Rev. 2014;20:523–
1074   44. https://doi.org/10.1089/ten.teb.2013.0664.

1075   2. Abbaszadeh H, Ghorbani F, Derakhshani M, Movassaghpour AA, Yousefi M, Talebi M, et al.
1076   Regenerative potential of Wharton's jelly-derived mesenchymal stem cells: A new horizon of stem cell
1077   therapy. J Cell Physiol. 2020;235:9230–40. https://doi.org/10.1002/jcp.29810.

1078   3. Lindner U, Kramer J, Rohwedel J, Schlenke P. Mesenchymal Stem or Stromal Cells: Toward a Better
1079   Understanding of Their Biology? Transfusion Medicine and Hemotherapy. 2010;37:75–83.
1080   https://doi.org/10.1159/000290897.

1081   4. Wong P-F, Dharmani M, Ramasamy TS. Senotherapeutics for mesenchymal stem cell senescence and
1082   rejuvenation. Drug Discov Today. 2023;28:103424. https://doi.org/10.1016/j.drudis.2022.103424.

1083   5. Oh J, Lee YD, Wagers AJ. Stem cell aging: mechanisms, regulators and therapeutic opportunities. Nat
1084   Med. 2014;20:870–80. https://doi.org/10.1038/nm.3651.

1085   6. Goodell MA, Rando TA. Stem cells and healthy aging. Science (1979). 2015;350:1199–204.
1086   https://doi.org/10.1126/science.aab3388.

1087   7. Carlos Sepúlveda J, Tomé M, Eugenia Fernández M, Delgado M, Campisi J, Bernad A, et al. Cell
1088   Senescence Abrogates the Therapeutic Potential of Human Mesenchymal Stem Cells in the Lethal
1089   Endotoxemia Model. Stem Cells. 2014;32:1865–77. https://doi.org/10.1002/stem.1654.

1090   8. Liu J, Ding Y, Liu Z, Liang X. Senescence in Mesenchymal Stem Cells: Functional Alterations, Molecular
1091   Mechanisms, and Rejuvenation Strategies. Front Cell Dev Biol. 2020;8.
1092   https://doi.org/10.3389/fcell.2020.00258.

1093   9. SETHE S, SCUTT A, STOLZING A. Aging of mesenchymal stem cells. Ageing Res Rev. 2006;5:91–116.
1094   https://doi.org/10.1016/j.arr.2005.10.001.

1095   10. Prišlin M, Butorac A, Bertoša R, Kunić V, Ljolje I, Kostešić P, et al. In vitro aging alters the gene
1096   expression and secretome composition of canine adipose-derived mesenchymal stem cells. Front Vet Sci.
1097   2024;11. https://doi.org/10.3389/fvets.2024.1387174.

1098   11. Amit M, Carpenter MK, Inokuma MS, Chiu C-P, Harris CP, Waknitz MA, et al. Clonally Derived Human
1099   Embryonic Stem Cell Lines Maintain Pluripotency and Proliferative Potential for Prolonged Periods of
1100   Culture. Dev Biol. 2000;227:271–8. https://doi.org/10.1006/dbio.2000.9912.

1101   12. Fehrer C, Laschober G, Lepperdinger G. Aging of murine mesenchymal stem cells. In: Annals of the
1102   New York Academy of Sciences. 2006. https://doi.org/10.1196/annals.1354.030.

1103   13. Bruder SP, Jaiswal N, Haynesworth SE. Growth kinetics, self-renewal, and the osteogenic potential of
1104   purified human mesenchymal stem cells during extensive subcultivation and following cryopreservation.
1105   J Cell Biochem. 1997;64:278–94. https://doi.org/10.1002/(SICI)1097-4644(199702)64:2<278::AID-
1106   JCB11>3.0.CO;2-F.

1107   14. Stenderup K. Aging is associated with decreased maximal life span and accelerated senescence of
1108   bone marrow stromal cells,. Bone. 2003;33:919–26. https://doi.org/10.1016/j.bone.2003.07.005.

1109   15. Trabucco SE, Zhang H. Finding Shangri-La: Limiting the Impact of Senescence on Aging. Cell Stem Cell.
1110   2016;18:305–6. https://doi.org/10.1016/j.stem.2016.02.002.

1111   16. Freund A, Laberge R-M, Demaria M, Campisi J. Lamin B1 loss is a senescence-associated biomarker.
1112   Mol Biol Cell. 2012;23:2066–75. https://doi.org/10.1091/mbc.e11-10-0884.

1113   17. Gardner SE, Humphry M, Bennett MR, Clarke MCH. Senescent Vascular Smooth Muscle Cells Drive
1114   Inflammation Through an Interleukin-1α–Dependent Senescence-Associated Secretory Phenotype.
1115   Arterioscler Thromb Vasc Biol. 2015;35:1963–74. https://doi.org/10.1161/ATVBAHA.115.305896.

1116   18. Acosta JC, Banito A, Wuestefeld T, Georgilis A, Janich P, Morton JP, et al. A complex secretory program
1117   orchestrated by the inflammasome controls paracrine senescence. Nat Cell Biol. 2013;15:978–90.
1118   https://doi.org/10.1038/ncb2784.

1119   19. Özcan S, Alessio N, Acar MB, Mert E, Omerli F, Peluso G, et al. Unbiased analysis of senescence
1120   associated secretory phenotype (SASP) to identify common components following different genotoxic
1121   stresses. Aging. 2016;8:1316–29. https://doi.org/10.18632/aging.100971.

1122   20. Demaria M, Ohtani N, Youssef SA, Rodier F, Toussaint W, Mitchell JR, et al. An Essential Role for
1123   Senescent Cells in Optimal Wound Healing through Secretion of PDGF-AA. Dev Cell. 2014;31:722–33.
1124   https://doi.org/10.1016/j.devcel.2014.11.012.

1125   21. Coppé J-P, Desprez P-Y, Krtolica A, Campisi J. The Senescence-Associated Secretory Phenotype: The
1126   Dark Side of Tumor Suppression. Annual Review of Pathology: Mechanisms of Disease. 2010;5:99–118.
1127   https://doi.org/10.1146/annurev-pathol-121808-102144.

1128   22. Biran A, Zada L, Abou Karam P, Vadai E, Roitman L, Ovadya Y, et al. Quantitative identification of
1129   senescent cells in aging and disease. Aging Cell. 2017;16:661–71. https://doi.org/10.1111/acel.12592.

1130   23. Schafer MJ, Zhang X, Kumar A, Atkinson EJ, Zhu Y, Jachim S, et al. The senescence-associated
1131   secretome as an indicator of age and medical risk. JCI Insight. 2020;5.
1132   https://doi.org/10.1172/jci.insight.133668.

1133   24. McKenzie BA. Comparative veterinary geroscience: mechanism of molecular, cellular, and tissue
1134   aging in humans, laboratory animal models, and companion dogs and cats. Am J Vet Res. 2022;83.
1135   https://doi.org/10.2460/ajvr.22.02.0027.

1136   25. Sándor S, Kubinyi E. Genetic Pathways of Aging and Their Relevance in the Dog as a Natural Model of
1137   Human Aging. Front Genet. 2019;10. https://doi.org/10.3389/fgene.2019.00948.

1138   26. Bruder SP, Jaiswal N, Haynesworth SE. Growth kinetics, self-renewal, and the osteogenic potential of
1139   purified human mesenchymal stem cells during extensive subcultivation and following cryopreservation.
1140   J Cell Biochem. 1997;64:278–94. https://doi.org/10.1002/(sici)1097-4644(199702)64:2<278::aid-
1141   jcb11>3.0.co;2-f.

1142   27. Lu LL, Liu YJ, Yang SG, Zhao QJ, Wang X, Gong W, et al. Isolation and characterization of human
1143   umbilical cord mesenchymal stem cells with hematopoiesis-supportive function and other potentials.
1144   Haematologica. 2006;91.

1145   28. Turinetto V, Vitale E, Giachino C. Senescence in Human Mesenchymal Stem Cells: Functional Changes
1146   and Implications in Stem Cell-Based Therapy. Int J Mol Sci. 2016;17:1164.
1147   https://doi.org/10.3390/ijms17071164.

1148   29. Khademi-Shirvan M, Ghorbaninejad M, Hosseini S, Baghaban Eslaminejad M. The Importance of
1149   Stem Cell Senescence in Regenerative Medicine. 2020. p. 87–102.
1150   https://doi.org/10.1007/5584_2020_489.

1151   30. Bertolo A, Baur M, Guerrero J, Pötzel T, Stoyanov J. Autofluorescence is a Reliable in vitro Marker of
1152   Cellular Senescence in Human Mesenchymal Stromal Cells. Sci Rep. 2019;9:2074.
1153   https://doi.org/10.1038/s41598-019-38546-2.

1154   31. Debacq-Chainiaux F, Erusalimsky JD, Campisi J, Toussaint O. Protocols to detect senescence-
1155   associated beta-galactosidase (SA-βgal) activity, a biomarker of senescent cells in culture and in vivo. Nat
1156   Protoc. 2009;4:1798–806. https://doi.org/10.1038/nprot.2009.191.

1157   32. Cohn RL, Gasek NS, Kuchel GA, Xu M. The heterogeneity of cellular senescence: insights at the single-
1158   cell level. Trends in Cell Biology. 2023;33. https://doi.org/10.1016/j.tcb.2022.04.011.

1159   33. Kriston-Pál É, Czibula Á, Gyuris Z, Balka G, Seregi A, Sükösd F, et al. Characterization and therapeutic
1160   application of canine adipose mesenchymal stem cells to treat elbow osteoarthritis. Canadian Journal of
1161   Veterinary Research. 2017;81.

1162   34. Pekker E, Priskin K, Szabó-Kriston É, Csányi B, Buzás-Bereczki O, Adorján L, et al. Development of a
1163   Large-Scale Pathogen Screening Test for the Biosafety Evaluation of Canine Mesenchymal Stem Cells. Biol
1164   Proced Online. 2023;25:33. https://doi.org/10.1186/s12575-023-00226-x.

1165   35. Andrews S, others. FastQC: a quality control tool for high throughput sequence data. 2010.
1166   Https://WwwBioinformaticsBabrahamAcUk/Projects/Fastqc/. 2019.

1167   36. Chen S, Zhou Y, Chen Y, Gu J. Fastp: An ultra-fast all-in-one FASTQ preprocessor. In: Bioinformatics.
1168   2018. https://doi.org/10.1093/bioinformatics/bty560.

1169 37. Bray NL, Pimentel H, Melsted P, Pachter L. Near-optimal probabilistic RNA-seq quantification. Nat
1170 Biotechnol. 2016;34. https://doi.org/10.1038/nbt.3519.

1171 38. Soneson C, Love MI, Robinson MD. Differential analyses for RNA-seq: transcript-level estimates
1172 improve gene-level inferences. F1000Res. 2015;4. https://doi.org/10.12688/f1000research.7563.1.

1173 39. Robinson MD, McCarthy DJ, Smyth GK. edgeR: A Bioconductor package for differential expression
1174 analysis of digital gene expression data. Bioinformatics. 2009;26.
1175 https://doi.org/10.1093/bioinformatics/btp616.

1176 40. Ritchie ME, Phipson B, Wu D, Hu Y, Law CW, Shi W, et al. Limma powers differential expression
1177 analyses for RNA-sequencing and microarray studies. Nucleic Acids Res. 2015;43.
1178 https://doi.org/10.1093/nar/gkv007.

1179 41. Wu T, Hu E, Xu S, Chen M, Guo P, Dai Z, et al. clusterProfiler 4.0: A universal enrichment tool for
1180 interpreting omics data. Innovation. 2021;2. https://doi.org/10.1016/j.xinn.2021.100141.

1181 42. Zheng GXY, Terry JM, Belgrader P, Ryvkin P, Bent ZW, Wilson R, et al. Massively parallel digital
1182 transcriptional profiling of single cells. Nat Commun. 2017;8. https://doi.org/10.1038/ncomms14049.

1183 43. Martin FJ, Amode MR, Aneja A, Austine-Orimoloye O, Azov AG, Barnes I, et al. Ensembl 2023. Nucleic
1184 Acids Res. 2023;51:D933–41. https://doi.org/10.1093/nar/gkac958.

1185 44. R Development Core Team. R Core Team (2020). R: A language and environment for statistical
1186 computing. R Foundation for Statistical Computing, Vienna, Austria. R Foundation for Statistical
1187 Computing. 2019;2.

1188 45. Hao Y, Hao S, Andersen-Nissen E, Mauck WM, Zheng S, Butler A, et al. Integrated analysis of
1189 multimodal single-cell data. Cell. 2021;184. https://doi.org/10.1016/j.cell.2021.04.048.

1190 46. Casella G, Munk R, Kim KM, Piao Y, De S, Abdelmohsen K, et al. Transcriptome signature of cellular
1191 senescence. Nucleic Acids Res. 2019;47. https://doi.org/10.1093/nar/gkz555.

1192 47. Wang Y, Liu L, Song Y, Yu X, Deng H. Unveiling E2F4, TEAD1 and AP-1 as regulatory transcription
1193 factors of the replicative senescence program by multi-omics analysis. Protein Cell. 2022;13.
1194 https://doi.org/10.1007/s13238-021-00894-z.

1195 48. Taherian Fard A, Leeson HC, Aguado J, Pietrogrande G, Power D, Gómez-Inclán C, et al.
1196 Deconstructing heterogeneity of replicative senescence in human mesenchymal stem cells at single cell
1197 resolution. Geroscience. 2024;46. https://doi.org/10.1007/s11357-023-00829-y.

1198 49. Lun ATL, Riesenfeld S, Andrews T, Dao TP, Gomes T, Marioni JC. EmptyDrops: Distinguishing cells from
1199 empty droplets in droplet-based single-cell RNA sequencing data. Genome Biol. 2019;20.
1200 https://doi.org/10.1186/s13059-019-1662-y.

1201 50. Korsunsky I, Millard N, Fan J, Slowikowski K, Zhang F, Wei K, et al. Fast, sensitive and accurate
1202 integration of single-cell data with Harmony. Nat Methods. 2019;16. https://doi.org/10.1038/s41592-
1203 019-0619-0.

1204 51. Wickham H. ggplot2: elegant graphics for data analysis. ht tp. had. co. nz/ggplot2/book . Springer;
1205 2009;8.

1206 52. Kevin Blighe, Sharmila Rana, Myles Lewis. EnhancedVolcano: publication-ready volcano plots with
1207 enhanced colouring and labeling. 2024.

1208 53. Guo X, Chen L. From G1 to M: a comparative study of methods for identifying cell cycle phases.
1209 Briefings in Bioinformatics. 2024;25. https://doi.org/10.1093/bib/bbad517.

1210 54. Tirosh I, Izar B, Prakadan SM, Wadsworth MH, Treacy D, Trombetta JJ, et al. Dissecting the
1211 multicellular ecosystem of metastatic melanoma by single-cell RNA-seq. Science (1979). 2016;352.
1212 https://doi.org/10.1126/science.aad0501.

1213 55. Wiley CD, Campisi J. The metabolic roots of senescence: mechanisms and opportunities for
1214 intervention. Nature Metabolism. 2021;3. https://doi.org/10.1038/s42255-021-00483-8.

1215 56. Deckx S, Heymans S, Papageorgiou AP. The diverse functions of osteoglycin: A deceitful dwarf, or a
1216 master regulator of disease. FASEB Journal. 2016;30. https://doi.org/10.1096/fj.201500096R.

1217 57. Freund A, Laberge R-M, Demaria M, Campisi J. Lamin B1 loss is a senescence-associated biomarker.
1218 Mol Biol Cell. 2012;23:2066–75. https://doi.org/10.1091/mbc.e11-10-0884.

1219 58. Hang Pham LB, Yoo YR, Park SH, Back SA, Kim SW, Bjørge I, et al. Investigating the effect of fibulin-1
1220 on the differentiation of human nasal inferior turbinate-derived mesenchymal stem cells into
1221 osteoblasts. J Biomed Mater Res A. 2017;105. https://doi.org/10.1002/jbm.a.36095.

1222 59. Limbad C, Doi R, McGirr J, Ciotlos S, Perez K, Clayton ZS, et al. Senolysis induced by 25-
1223 hydroxycholesterol targets CRYAB in multiple cell types. iScience. 2022;25.
1224 https://doi.org/10.1016/j.isci.2022.103848.

1225 60. Zou H, Stoppani E, Volonte D, Galbiati F. Caveolin-1, cellular senescence and age-related diseases.
1226 Mech Ageing Dev. 2011;132. https://doi.org/10.1016/j.mad.2011.11.001.

1227 61. Cooley MA, Harikrishnan K, Oppel JA, Miler SF, Barth JL, Haycraft CJ, et al. Fibulin-1 is required for
1228 bone formation and Bmp-2-mediated induction of Osterix. Bone. 2014;69:30–8.
1229 https://doi.org/10.1016/j.bone.2014.07.038.

1230 62. Zhang D, Liu X, Xu X, Xu J, Yi Z, Shan B, et al. HPCAL1 promotes glioblastoma proliferation via
1231 activation of Wnt/β-catenin signalling pathway. J Cell Mol Med. 2019;23.
1232 https://doi.org/10.1111/jcmm.14083.

1233 63. Lee BC, Yu KR. Impact of mesenchymal stem cell senescence on inflammaging. BMB Reports.
1234 2020;53. https://doi.org/10.5483/BMBRep.2020.53.2.291.

1235 64. Hao M, Jiang H, Zhao Y, Li C, Jiang J. Identification of potential biomarkers for aging diagnosis of
1236 mesenchymal stem cells derived from the aged donors. Stem Cell Res Ther. 2024;15.
1237 https://doi.org/10.1186/s13287-024-03689-1.

1238 65. Ruple A, Maclean E, Snyder-Mackler N, Creevy KE, Promislow D. Dog Models of Aging. Annual Review
1239 of Animal Biosciences. 2022;10. https://doi.org/10.1146/annurev-animal-051021-080937.

1240 66. Hardwick LJA, Kortum AJ, Constantino-Casas F, Watson PJ. Breed-related expression patterns of Ki67,
1241 γH2AX, and p21 during ageing in the canine liver. Vet Res Commun. 2021;45.
1242 https://doi.org/10.1007/s11259-020-09784-x.

1243 67. Sándor S, Jónás D, Tátrai K, Czeibert K, Kubinyi E. Poly(A) RNA sequencing reveals age-related
1244 differences in the prefrontal cortex of dogs. Geroscience. 2022;44. https://doi.org/10.1007/s11357-022-
1245 00533-3.

1246 68. Mirsaidi A, Kleinhans KN, Rimann M, Tiaden AN, Stauber M, Rudolph KL, et al. Telomere length,
1247 telomerase activity and osteogenic differentiation are maintained in adipose-derived stromal cells from
1248 senile osteoporotic SAMP6 mice. J Tissue Eng Regen Med. 2012;6. https://doi.org/10.1002/term.440.

1249 69. Melk A, Schmidt BMW, Takeuchi O, Sawitzki B, Rayner DC, Halloran PF. Expression of p16INK4a and
1250 other cell cycle regulator and senescence associated genes in aging human kidney. Kidney Int. 2004;65.
1251 https://doi.org/10.1111/j.1523-1755.2004.00438.x.

1252 70. Zindy F, Quelle DE, Roussel MF, Sherr CJ. Expression of the p16(INK4a) tumor suppressor versus other
1253 INK4 family members during mouse development and aging. Oncogene. 1997;15.
1254 https://doi.org/10.1038/sj.onc.1201178.

1255 71. Bertolo A, Steffen F, Malonzo-Marty C, Stoyanov J. Canine mesenchymal stem cell potential and the
1256 importance of dog breed: Implication for cell-based therapies. Cell Transplant. 2015;24.
1257 https://doi.org/10.3727/096368914X685294.

1258 72. A B. Comparative Characterization of Canine and Human Mesenchymal Stem Cells Derived from Bone
1259 Marrow. Int J Stem Cell Res Ther. 2015;2. https://doi.org/10.23937/2469-570x/1410005.

1260 73. Li Y, Wu Q, Yujia W, Li L, Bu H, Bao J. Senescence of mesenchymal stem cells (Review). Int J Mol Med.
1261 2017;39. https://doi.org/10.3892/ijmm.2017.2912.

1262 74. Zhou S, Greenberger JS, Epperly MW, Goff JP, Adler C, Leboff MS, et al. Age-related intrinsic changes
1263 in human bone-marrow-derived mesenchymal stem cells and their differentiation to osteoblasts. Aging
1264 Cell. 2008;7. https://doi.org/10.1111/j.1474-9726.2008.00377.x.

1265 75. Wang D, Xiao F, Feng Z, Li M, Kong L, Huang L, et al. Sunitinib facilitates metastatic breast cancer
1266 spreading by inducing endothelial cell senescence. Breast Cancer Research. 2020;22.
1267 https://doi.org/10.1186/s13058-020-01346-y.

1268 76. Belcastro E, Rehman AU, Remila L, Park SH, Gong DS, Anton N, et al. Fluorescent nanocarriers
1269 targeting VCAM-1 for early detection of senescent endothelial cells. Nanomedicine. 2021;34.
1270 https://doi.org/10.1016/j.nano.2021.102379.

1271 77. Alves H, van Ginkel J, Groen N, Hulsman M, Mentink A, Reinders M, et al. A mesenchymal stromal cell
1272 gene signature for donor age. PLoS One. 2012;7. https://doi.org/10.1371/journal.pone.0042908.

1273 78. Chelombitko MA, Morgunova G V., Strochkova NY, Zinovkin RA, Pavlyuchenkova AN, Kondratenko ND,
1274 et al. Comparative Analysis of Cell Senescence Induced by the Chemotherapeutic Agents Doxorubicin,
1275 Cisplatin and Arsenic Trioxide in Human Myoblasts MB135. Advances in Gerontology. 2023;13.
1276 https://doi.org/10.1134/S2079057024600010.

1277 79. Li M, Ren H, Zhang Y, Liu N, Fan M, Wang K, et al. MECOM/PRDM3 and PRDM16 Serve as Prognostic-
1278 Related Biomarkers and Are Correlated With Immune Cell Infiltration in Lung Adenocarcinoma. Front
1279 Oncol. 2022;12. https://doi.org/10.3389/fonc.2022.772686.

1280 80. Bryant AG, Hu M, Carlyle BC, Arnold SE, Frosch MP, Das S, et al. Cerebrovascular Senescence Is
1281 Associated With Tau Pathology in Alzheimer's Disease. Front Neurol. 2020;11.
1282 https://doi.org/10.3389/fneur.2020.575953.

1283 81. Qin Z, Chen Z, Weng J, Li S, Rong Z, Zhou C. Elevated HOXA13 expression promotes the proliferation
1284 and metastasis of gastric cancer partly via activating Erk1/2. Onco Targets Ther. 2019;12.
1285 https://doi.org/10.2147/OTT.S196986.

1286 82. Yu M, Zhan J, Zhang H. HOX family transcription factors: Related signaling pathways and post-
1287 translational modifications in cancer. Cellular Signalling. 2020;66.
1288 https://doi.org/10.1016/j.cellsig.2019.109469.

1289 83. Lee J, Kim YS, Kim E, Kim Y, Kim Y. Curcumin and hesperetin attenuate d-galactose-induced brain
1290 senescence in vitro and in vivo. Nutr Res Pract. 2020;14. https://doi.org/10.4162/nrp.2020.14.5.438.

1291 84. Bérubé NG, Swanson XH, Bertram MJ, Kittle JD, Didenko V, Baskin DS, et al. Cloning and
1292 characterization of CRF, a novel C1q-related factor, expressed in areas of the brain involved in motor
1293 function. Molecular Brain Research. 1999;63. https://doi.org/10.1016/S0169-328X(98)00278-2.

1294 85. Qiu X, Feng JR, Wang F, Chen PF, Chen XX, Zhou R, et al. Profiles of differentially expressed genes and
1295 overexpression of NEBL indicates a positive prognosis in patients with colorectal cancer. Mol Med Rep.
1296 2018;17. https://doi.org/10.3892/mmr.2017.8210.

1297 86. Ni F, Wang F, Li J, Liu Y, Sun X, Chen J, et al. BNC1 deficiency induces mitochondrial dysfunction-
1298 triggered spermatogonia apoptosis through the CREB/SIRT1/FOXO3 pathway: the therapeutic potential
1299 of nicotinamide riboside and metformin. Biol Reprod. 2024;110. https://doi.org/10.1093/biolre/ioad168.

1300 87. Short SP, Pilat JM, Barrett CW, Reddy VK, Haberman Y, Hendren JR, et al. Colonic Epithelial-Derived
1301 Selenoprotein P Is the Source for Antioxidant-Mediated Protection in Colitis-Associated Cancer.
1302 Gastroenterology. 2021;160. https://doi.org/10.1053/j.gastro.2020.12.059.

1303 88. Koral K, Paranjpe S, Bowen WC, Mars W, Luo J, Michalopoulos GK. Leukocyte-Specific Protein 1: A
1304 novel regulator of hepatocellular proliferation and migration deleted in human hepatocellular
1305 carcinoma. Hepatology. 2015;61. https://doi.org/10.1002/hep.27444.

1306 89. Zhang H, Okuyama H, Jain A, Jadhav RR, Wu B, Sturmlechner I, et al. PREX1 improves homeostatic
1307 proliferation to maintain a naive CD4+ T cell compartment in older age. JCI Insight. 2024;9.
1308 https://doi.org/10.1172/jci.insight.172848.

1309 90. de Resende MF, Vieira S, Chinen LTD, Chiappelli F, da Fonseca FP, Guimarães GC, et al. Prognostication
1310 of prostate cancer based on TOP2A protein and gene assessment: TOP2A in prostate cancer. J Transl
1311 Med. 2013;11. https://doi.org/10.1186/1479-5876-11-36.

1312 91. Musa J, Aynaud MM, Mirabeau O, Delattre O, Grünewald TGP. MYBL2 (B-Myb): a central regulator of
1313 cell proliferation, cell survival and differentiation involved in tumorigenesis. Cell Death and Disease.
1314 2017;8. https://doi.org/10.1038/CDDIS.2017.244.

1315 92. Liu ZM, Bao Y, Li TK, Di Y Bin, Song WJ. MKI67 an potential oncogene of oral squamous cell carcinoma
1316 via the high throughput technology. Medicine (United States). 2022;101.
1317 https://doi.org/10.1097/MD.0000000000032595.

93. Xi LC, Ji YX, Yin D, Zhao ZX, Huang SC, Yu SL, et al. Effects of Dermatopontin gene silencing on apoptosis and proliferation of osteosarcoma MG-63 cells. Mol Med Rep. 2018;17. https://doi.org/10.3892/mmr.2017.7866.

94. Shandilya J, Roberts SGE. A role of WT1 in cell division and genomic stability. Cell Cycle. 2015;14. https://doi.org/10.1080/15384101.2015.1021525.

95. Tang C, Qiu S, Mou W, Xu J, Wang P. Excessive activation of HOXB13/PIMREG axis promotes hepatocellular carcinoma progression and drug resistance. Biochem Biophys Res Commun. 2022;623. https://doi.org/10.1016/j.bbrc.2022.07.066.

96. Chatsirisupachai K, Palmer D, Ferreira S, de Magalhães JP. A human tissue-specific transcriptomic analysis reveals a complex relationship between aging, cancer, and cellular senescence. Aging Cell. 2019;18. https://doi.org/10.1111/acel.13041.

97. Gruber HE, Hoelscher GL, Ingram JA, Zinchenko N, Hanley EN. Senescent vs. non-senescent cells in the human annulus in vivo: Cell harvest with laser capture microdissection and gene expression studies with microarray analysis. BMC Biotechnol. 2010;10. https://doi.org/10.1186/1472-6750-10-5.

98. Wagner W, Horn P, Castoldi M, Diehlmann A, Bork S, Saffrich R, et al. Replicative senescence of mesenchymal stem cells: A continuous and organized process. PLoS One. 2008;3. https://doi.org/10.1371/journal.pone.0002213.

99. Zou J, Lei T, Guo P, Yu J, Xu Q, Luo Y, et al. Mechanisms shaping the role of ERK1/2 in cellular senescence (Review). Mol Med Rep. 2019;19. https://doi.org/10.3892/mmr.2018.9712.

100. Fujita M, Sasada M, Iyoda T, Fukai F. Involvement of Matricellular Proteins in Cellular Senescence: Potential Therapeutic Targets for Age-Related Diseases. International Journal of Molecular Sciences. 2024;25. https://doi.org/10.3390/ijms25126591.

101. Yeo EJ. Hypoxia and aging. Experimental and Molecular Medicine. 2019;51. https://doi.org/10.1038/s12276-019-0233-3.

102. Xu W, Liu X, Han W, Wu K, Zhao M, Mei T, et al. Inhibiting HIF-1 signaling alleviates HTRA1-induced RPE senescence in retinal degeneration. Cell Communication and Signaling. 2023;21. https://doi.org/10.1186/s12964-023-01138-9.

103. Sun Y, Yu X, Gao X, Zhang C, Sun H, Xu K, et al. RNA sequencing profiles reveal dynamic signaling and glucose metabolic features during bone marrow mesenchymal stem cell senescence. Cell Biosci. 2022;12. https://doi.org/10.1186/s13578-022-00796-5.

104. Nassrally MS, Lau A, Wise K, John N, Kotecha S, Lee KL, et al. Cell cycle arrest in replicative senescence is not an immediate consequence of telomere dysfunction. Mech Ageing Dev. 2019;179. https://doi.org/10.1016/j.mad.2019.01.009.

105. Perez K, Ciotlos S, McGirr J, Limbad C, Doi R, Nederveen JP, et al. Single nuclei profiling identifies cell specific markers of skeletal muscle aging, frailty, and senescence. Aging. 2022;14. https://doi.org/10.18632/aging.204435.

1354 106. Moussavi-Harami F, Duwayri Y, Martin JA, Moussavi-Harami F, Buckwalter JA. Oxygen effects on
1355 senescence in chondrocytes and mesenchymal stem cells: consequences for tissue engineering. Iowa
1356 Orthop J. 2004;24.

1357 107. Kawamura H, Nakatsuka R, Matsuoka Y, Sumide K, Fujioka T, Asano H, et al. TGF-β Signaling
1358 Accelerates Senescence of Human Bone-Derived CD271 and SSEA-4 Double-Positive Mesenchymal
1359 Stromal Cells. Stem Cell Reports. 2018;10. https://doi.org/10.1016/j.stemcr.2018.01.030.

1360 108. Volonte D, Galbiati F. Caveolin-1, a master regulator of cellular senescence. Cancer and Metastasis
1361 Reviews. 2020;39. https://doi.org/10.1007/s10555-020-09875-w.

1362 109. Fittipaldi S, Mercatelli N, Dimauro I, Jackson MJ, Paronetto MP, Caporossi D. Alpha B-crystallin
1363 induction in skeletal muscle cells under redox imbalance is mediated by a JNK-dependent regulatory
1364 mechanism. Free Radic Biol Med. 2015;86. https://doi.org/10.1016/j.freeradbiomed.2015.05.035.

1365 110. Masamha CP, Benbrook DM. Cyclin D1 degradation is sufficient to induce G1 cell cycle arrest despite
1366 constitutive expression of cyclin E2 in ovarian cancer cells. Cancer Res. 2009;69.
1367 https://doi.org/10.1158/0008-5472.CAN-09-0913.

1368 111. Leontieva O V., Demidenko ZN, Blagosklonny M V. MEK drives cyclin D1 hyperelevation during
1369 geroconversion. Cell Death Differ. 2013;20. https://doi.org/10.1038/cdd.2013.86.

1370 112. Pagano M, Theodoras AM, Tam SW, Draetta GF. Cyclin D1-mediated inhibition of repair and
1371 replicative DNA synthesis in human fibroblasts. Genes Dev. 1994;8.
1372 https://doi.org/10.1101/gad.8.14.1627.

1373 113. Duangprom S, Kheolamai P, Tantrawatpan C, Manochantr S. High glucose inhibits proliferation,
1374 migration, and osteogenic differentiation of human placenta-derived mesenchymal stem cells. Sci Rep.
1375 2025;15. https://doi.org/10.1038/s41598-025-06454-3.

1376 114. Laphanuwat P, Likasitwatanakul P, Sittithumcharee G, Thaphaengphan A, Chomanee N, Suppramote
1377 O, et al. Cyclin D1 depletion interferes with oxidative balance and promotes cancer cell senescence. J Cell
1378 Sci. 2018;131. https://doi.org/10.1242/jcs214726.

1379 115. Jazbutyte V, Fiedler J, Kneitz S, Galuppo P, Just A, Holzmann A, et al. MicroRNA-22 increases
1380 senescence and activates cardiac fibroblasts in the aging heart. Age (Omaha). 2013;35.
1381 https://doi.org/10.1007/s11357-012-9407-9.

1382 116. Chen X, Chen J, Xu D, Zhao S, Song H, Peng Y. Effects of Osteoglycin (OGN) on treating senile
1383 osteoporosis by regulating MSCs. BMC Musculoskelet Disord. 2017;18. https://doi.org/10.1186/s12891-
1384 017-1779-7.

1385

1386

1387

1388 **Figure legends**

1389 **Figure 1 Senescence-associated β-galactosidase assay. A**. Schematic representation of the

1390 workflow for the detection of senescence-associated β-galactosidase. P2 and P6 cells (10^5) were

1391 cultured in triplicates in 6-well plates for 24 hours, fixed with 8% paraformaldehyde for 10

1392 minutes, and washed with distilled water. Cells were stained with SPiDER-βGal solution (diluted

1393 1:2000 in McIlvaine buffer, pH 6.0). Nuclei were then stained with DAPI, and cells were

1394 observed using a Leica Stellaris laser scanning confocal microscope. **B.** Representative images of

1395 senescence-associated-β-galactosidase (SA-β-gal) staining assay. Scale bar is 50 µm **C.**

1396 Quantitative fluorescence intensity data were obtained from 35 cells, measuring two cytoplasmic

1397 regions per cell, resulting in a total of 70 measurements per replicate. The boxplot whiskers

1398 extend from the third and first quartiles to the largest and smallest values, respectively, within 1.5

1399 x the interquartile range (IQR), where IQR represents the range between the first and third

1400 quartiles.

1401 The observed difference in fluorescence intensity was considered statistically significant, with a

1402 p-value <2.2e-16.

1403 **Figure 2 Bulk RNA sequencing-based transcriptomic analysis. A.** Schematic representation

1404 of the workflow for bulk RNA seq-based assay**.** MSCs were collected from six consecutive cell

1405 passages. P2- and P6-derived cells were selected for the study. Bulk RNA sequencing of P2- and

1406 P6-derived cells was carried out in triplicates, following RNA extraction and library preparation

1407 using Illumina NextSeq 500, and the results were analysed bioinformatically. **B.** Volcano plot

1408 highlighting the top identified DEGs in P6-derived samples, compared to P2 samples. Red data

1409 points indicate those genes that were significantly upregulated (right) or downregulated (left). X-

1410 axis=Log_2FC, horizontal dashed line indicates cutoff for P-value<0.01, while the vertical dashed

1411 lines indicate the cutoff for fold change of 2. **C.** Results of GO enrichment analysis for the

1412 downregulated differentially expressed genes. X-axis = Fold enrichment values. Y-axis=relevant

1413 enriched GO terms for different biological processes; colour intensity of bars based on p-value.

1414 **D.** Results of GO enrichment analysis for the upregulated differentially expressed genes. X-axis

1415 = Fold enrichment values. Y-axis=relevant enriched GO terms for different biological processes;

1416 colour intensity of bars based on p-value.

1417 **Figure 3 Single-cell RNA sequencing workflow and UMAP clustering analysis of cells**

1418 **derived from P2 and P6. A.** MSCs were collected from six consecutive cell passages, and P2-

1419 and P6-derived cells were selected for the study. Single-cell RNA sequencing of the cells was

1420 carried out using Single Cell 3′ GEM, Library & Gel Bead Kit v3.1 with the generated mRNA

1421 libraries sequenced using the Illumina NovaSeqX Plus system, and the results analysed

1422 bioinformatically. **B.** Distribution of the identified clusters. **C.** Distribution of the clusters based

1423 on the origin of the sample (P2= Passage 2, P6= Passage 6).

1424 **Figure 4 Cell cycle stages and proliferation dynamics within the clusters. A.** The cell cycle of

1425 the sorted cells was assessed by flow cytometry using propidium iodide staining. Representative

1426 images of P2 (left) and P6 (right) cells are shown, highlighting that P6 cells are represented by a

1427 considerably higher proportion of cells in the G1 phase. **B-C**. Cell cycle stages of the cell

1428 population and percentages are displayed separately for P2 (left) and P6 (right), as determined by

1429 Cell Scoring analysis using the Seurat package. **D**. Feature plot representing the expression of

1430 proliferation marker PLK1 among the clusters. Inset on the right highlights cluster distribution **E.**

1431 Expression of transcripts for cell proliferation markers and division regulators PLK1, MKI67,

1432 MCM3, and MCM6. The clusters are arranged based on the origin of the sample (P2 followed by

1433 P6).

Figure 5 Evaluation of the significantly enriched GO terms, emphasizing three critical pathways associated with cellular senescence at the single-cell level. **A.** the ERK1 and ERK2 cascade: feature plot illustrating the expression of the APP gene (top), violin plots showing the expression levels of the ERK1 and ERK2 cascade-related genes APP, EDN1, and CCL5 among the clusters (bottom). **B**. Integrin-mediated signalling pathway: feature plot illustrating the expression of the TIMP1 gene (top), violin plots showing the expression levels of the integrin-mediated signalling pathway-related genes TIMP1, ITGA1, and ITGA2 (bottom). **C.** Response to oxygen levels: feature plot illustrating the expression of the CRYAB gene (top), violin plots showing the expression levels of response to oxygen levels GO term-related genes EDN1, CRYAB and TGFB2 (bottom). The clusters are arranged based on the origin of the sample (P2 followed by P6).

Figure 6 Characterization of cluster-specific markers and assessment of transcriptional patterns of genes associated with cellular senescence. A. Heatmap showing the top five highly expressed marker RNAs in each cluster (based on LogFC). Cluster6*: Genes KRT3 and IL1RL1 appear in the top five marker list for both cluster 4 and cluster 6. To avoid redundancy and potential confusion, the expression values of these genes were visualized under cluster 4 and were excluded from the visualization for cluster 6. Median expression levels were plotted for cells in each cluster. Colour represents expression intensity (based on LogFC value). The clusters are arranged based on the origin of the sample (P2 followed by P6), whereas the genes are arranged based on cluster order from cluster 0 to 7. **B.** Dotplot depicting markers commonly associated with cellular senescence, with dot colour representing the average RNA expression levels scaled across all clusters. The size of each dot indicates the percentage of cells expressing a specific RNA within each cluster. The clusters are arranged based on the origin of the sample

1457 (P2 followed by P6). **C.** Violin plot depicting the expression of LMNB1. **D.** Feature plot

1458 depicting the expression of CCND1. **E.** Violin plot showing the expression level of CCND1 for

1459 each cluster. The clusters are arranged based on the origin of the sample (P2 followed by P6).

1460 **Figure 7 Analysis of top marker genes in late-passage cell populations and characterisation**

1461 **of CRYAB interacting partners. A.** Heatmap showing the expression of the top ten marker

1462 genes in late-passage cell populations. Each line represents a single cell, the colour indicates the

1463 expression level (pink – downregulated, yellow – overexpressed). The clusters are arranged

1464 based on the origin of the sample (P2 followed by P6). **B.** Ridge plot of CRYAB expression and

1465 its interacting partners APP, HSPB1, and HSPB2. **C.** Bar graph displaying the percentage of

1466 senescent cells across clusters, based on gene co-occurrence analysis. The analysis includes both

1467 established senescence markers and newly identified genes that may serve as potential novel

1468 markers of cellular senescence. The clusters are arranged based on the origin of the sample (P2

1469 followed by P6).

1470